



Frequency capture phenomenon in tandem cylinders with different diameters undergoing flow-induced vibration

Cite as: Phys. Fluids **34**, 085120 (2022); <https://doi.org/10.1063/5.0101780>

Submitted: 03 June 2022 • Accepted: 21 July 2022 • Accepted Manuscript Online: 21 July 2022 •
Published Online: 12 August 2022

 Xuepeng Fu (付雪鹏),  Shixiao Fu (付世晓), Mengmeng Zhang (张萌萌), et al.



View Online



Export Citation



CrossMark

ARTICLES YOU MAY BE INTERESTED IN

[Flexible cylinder flow-induced vibration](#)

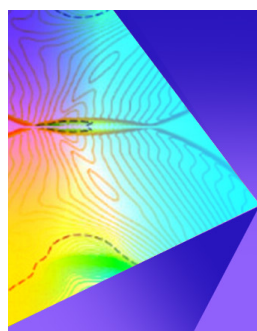
Physics of Fluids **34**, 011302 (2022); <https://doi.org/10.1063/5.0078418>

[Fluid-thermal-structure interaction of three heated circular cylinders in tandem at a low Reynolds number of 150](#)

Physics of Fluids **34**, 083605 (2022); <https://doi.org/10.1063/5.0105014>

[Spacing effect on the vortex-induced vibrations of near-wall flexible cylinders in the tandem arrangement](#)

Physics of Fluids **34**, 097123 (2022); <https://doi.org/10.1063/5.0115954>



Physics of Fluids

Special Topic: Shock Waves

Submit Today!

Frequency capture phenomenon in tandem cylinders with different diameters undergoing flow-induced vibration

Cite as: Phys. Fluids **34**, 085120 (2022); doi: 10.1063/5.0101780

Submitted: 3 June 2022 · Accepted: 21 July 2022 ·

Published Online: 12 August 2022



View Online



Export Citation



CrossMark

Xuepeng Fu (付雪鹏),^{1,2}  Shixiao Fu (付世晓),^{1,2,a)}  Mengmeng Zhang (张萌萌),^{1,2} Zhaolong Han (韩兆龙),^{1,2}  Haojie Ren (任浩杰),^{1,2} Yuwang Xu (许玉旺),^{1,2} and Bing Zhao (赵冰)^{1,2}

AFFILIATIONS

¹State Key Laboratory of Ocean Engineering, Shanghai Jiao Tong University, Shanghai 200240, China

²Institute of Polar and Ocean Technology, Institute of Marine Equipment, Shanghai Jiao Tong University, Shanghai 200240, China

^{a)}Author to whom correspondence should be addressed: shixiao.fu@sjtu.edu.cn

ABSTRACT

A frequency capture phenomenon in which the dominant response frequency of the downstream cylinder is the same as that of the upstream cylinder despite the differences in their physical characteristics was recently experimentally identified. The mechanism of this phenomenon is investigated by flow around two cylinders with unequal diameters undergoing flow-induced vibrations (FIV) using the open-source code OpenFOAM. Two FIV systems, a large stationary/vibrating upstream cylinder and vibrating downstream cylinder, are used for the simulation. The cylinders are free to vibrate in both the in-line and cross-flow directions. The forgetting factor least squares algorithm is applied for the time-varying excitation mechanism analysis. Simulation results show that the response of the downstream cylinder has a larger amplitude and contains multi-frequency components than the vortex-induced vibration of an isolated cylinder, making its trajectory more complicated. Simulations confirm that the frequency capture phenomenon is induced by the action of the upstream shedding vortex on the downstream cylinder. The energy transfers from vorticity to the structure when the frequency capture phenomenon occurs. The response of the downstream cylinder comprises a significant component of the vortex shedding frequency of the upstream cylinder.

Published under an exclusive license by AIP Publishing. <https://doi.org/10.1063/5.0101780>

I. INTRODUCTION

Elastically mounted cylinders in tandem arrangements are widely used in ocean engineering, such as subsea pipelines and risers. This type of engineering equipment is impacted by alternating vortex shedding generated by ocean currents. Vortex-induced vibration (VIV) has been confirmed as a significant factor of fatigue damage and may magnify the drag forces of slender flexible structures. In ocean engineering, slender flexible structures with unequal diameters are always arranged in bundles and bundled together during subsea wellhead maintenance, and for the subsea pipeline overhang section, production risers with small diameters and drilling risers with large diameters are arranged side by side. The downstream cylinder will be affected by the wake induced by the upstream cylinder and will exhibit a complicated vibration characteristic known as wake-induced vibration (WIV). VIV and WIV are both induced by flow and referred to as flow-induced vibrations (FIV).

The study of VIV was started by investigating the response characteristics of an isolated elastically mounted bluff cylinder and a

flexible cylinder. The VIV of an isolated elastically mounted bluff cylinder in the cross flow (CF) and in-line (IL)–CF combined directions was studied. Many critical parameters and phenomena have been proposed and identified that have enriched our fundamental knowledge of VIV.^{1–3} The VIV of a flexible cylinder is characterized by multi-mode and multi-frequency vibrations different from those of a bluff cylinder. However, the bluff cylinder system has been widely used to investigate the fundamental VIV mechanism, and the related research results have been widely used in the piratical flexible cylinder VIV prediction.^{4,5} These issues have been widely studied over five decades, and many reviews have been published.^{6–16}

Research on flow around tandem cylinders with equal diameters paves the way for tandem system studies. Three schemes of flow patterns for two tandem circular cylinders have been classified: the extended-body regime, the reattachment regime, and the co-shedding regime,^{17,18} as shown in Fig. 1. Furthermore, a WIV system with a fixed upstream cylinder and an elastically attached downstream cylinder was investigated. Assi¹⁹ investigated the mechanism of a WIV of a

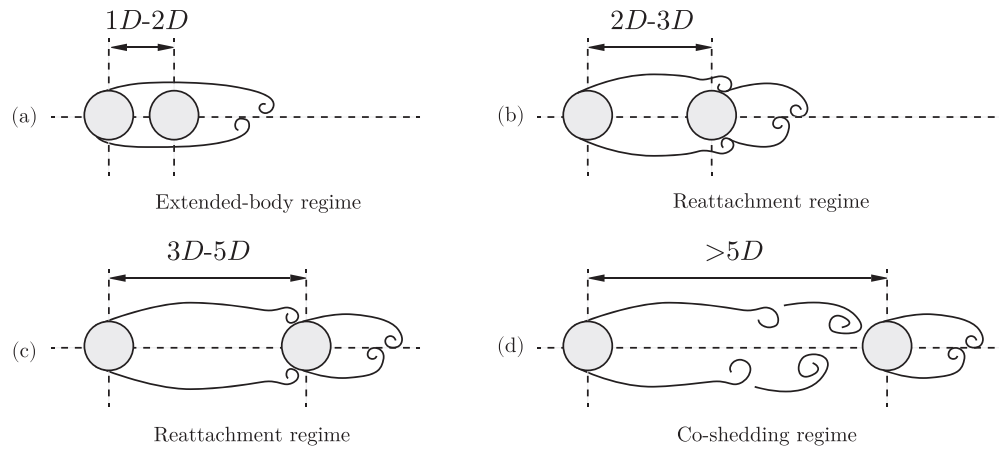


FIG. 1. Simplified classification scheme of the flow patterns for two tandem circular cylinders: (a) extended-body regime, (b) and (c) reattachment regime, and (d) co-shedding regime.

pair of cylinders in tandem with vibrating downstream cylinders in one degree of freedom (1DOF) (CF only). Furthermore, Assi²⁰ performed further WIV tests with vibrating a downstream cylinder in 2DOFs and demonstrated that the vortex excitation mechanism of unsteady wake–structure interactions provides positive energy for the downstream cylinder undergoing WIV. Shan²¹ conducted a numerical study of tandem cylinders with different diameters at low *Re*.

The mechanism of tandem cylinders with both vibrating upstream and downstream cylinders is more complex. Kim *et al.*²² experimentally studied WIV with vibrating upstream and downstream cylinders in 1DOF and proposed five regimes based on the vibration responses. Ding *et al.*²³ proposed two-dimensional unsteady Reynolds-averaged Navier–Stokes (2D URANS) simulations of WIV with vibrating upstream and downstream cylinders in 1DOF. For flexible cylinder systems, Huera-Huarte and Bearman²⁴ conducted experiments on WIV with two flexible cylinders having the same diameter. The experiment showed that the upstream cylinder experiences larger vibrations than the downstream cylinder when the gap spacing is small, but for a large gap spacing, the downstream cylinder undergoes nonclassical VIV or WIV with large amplitudes at a high reduced velocity. Wu *et al.*²⁵ investigated the flow-induced vibration of two tandem cylinders in a cluster.

There has been little investigation into a tandem system with two cylinders with different diameters both undergoing FIV. Huang and Sworn²⁶ carried out WIV experiments of two bluff cylinders with different diameters in 2DOFs. The results show that the trajectories are qualitatively different between the upstream cylinder in steady uniform flow and the downstream cylinder situated in the wake of the upstream cylinder. Xu *et al.*²⁷ conducted an FIV experiment with a flexible large upstream cylinder and small downstream cylinder and proposed that the increase in the upstream cylinder diameter would make the WIV of the downstream cylinder more complicated. Janocha *et al.*²⁸ simulate the FIV of a bluff large upstream cylinder and small downstream cylinder using URANS.

Our research team recently conducted interference experiments of dual flexible pipes in the subcritical *Re* range¹¹ [*Re* ~ $O(10^4)$] with a large upstream cylinder diameter in a tandem arrangement and

discovered that the downstream small diameter pipe’s dominant response frequency equals the response frequency of the upstream large diameter pipe, which is named the *frequency capture phenomenon*.²⁹ This phenomenon was also found in the URANS simulations of bluff cylinders with unequal diameters in 1DOF.³⁰ However, in actual ocean engineering, slender structures, such as risers, vibrate in 2DOF motion. The mechanism analysis with a 2DOF system is still unknown.

In the present study, we extend the simulation to 2DOF motion and study the mechanisms of the frequency capture phenomenon. Two kinds of FIV systems are defined: a stationary large upstream cylinder and vibrating small downstream cylinder and a vibrating large upstream cylinder and small downstream cylinder. The reduced velocity based on the downstream cylinder reached 22.25. Simulation results confirm that the frequency capture phenomenon is induced by the action of the upstream shedding vortex on the downstream cylinder. The energy transfers from vorticity to the structure when the frequency capture phenomenon occurs. The response of the downstream cylinder comprises a significant component of the vortex shedding frequency of the upstream cylinder. Furthermore, the response of the downstream cylinder has a larger amplitude and contains multifrequency components than the VIV of an isolated cylinder, making its trajectory more complicated.

II. MATHEMATICAL FORMULATION

A. Flow model

The governing equations are the 2D Navier–Stokes (N–S) equations, which, written in the Cartesian coordinate system, are the following:

$$\frac{\partial u_i}{\partial x_i} = 0, \tag{1}$$

$$\frac{\partial u_i}{\partial t} + u_j \frac{\partial u_i}{\partial x_j} = -\frac{1}{\rho} \frac{\partial p}{\partial x_i} + \nu \frac{\partial^2 u_i}{\partial x_j \partial x_j}, \tag{2}$$

where $i, j = 1, 2$; x_1 and x_2 denote the streamwise (in-line, IL) and cross-stream (cross flow, CF) directions, respectively; u_1 and u_2 are the

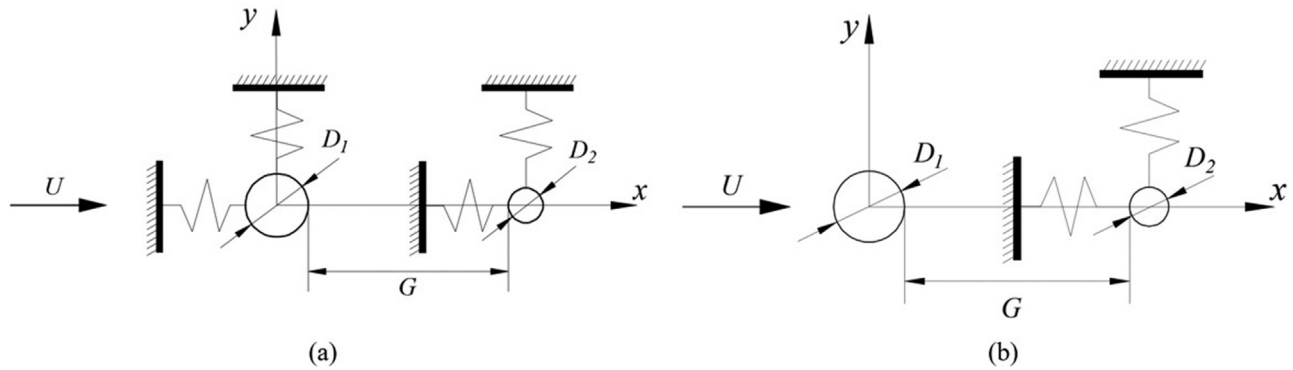


FIG. 2. Schematic of VIVs of elastically mounted cylinders: (a) two elastically mounted cylinders (system 1) and (b) stationary upstream cylinder and elastically mounted downstream cylinder (system 2).

corresponding velocity components; ρ is the density of the fluid; and p is the pressure.

The finite volume method (FVM)-based open-source CFD code OpenFOAM is used in the present study to solve the N–S equation. The shear stress transport (SST) $k - \omega$ turbulent model³¹ is used. The pressure–velocity coupling equation is established using the PIMPLE algorithm, which combines both the PISO and SIMPLE algorithms, thus enhancing the accuracy of the numerical simulations, especially when using large time steps in a moving mesh. All the employed spatial schemes are of second-order accuracy. The implicit Euler scheme is used for the time integration.

The pressure equation is solved by using a geometric-algebraic multigrid (GAMG) iterative solver with the Gauss–Seidel smoother. The unsteady simulation is solved with time step $0.003 \cdot D/U$ with Courant number³² $Co < 0.8$.

B. Structural model

In the present study, two mass-damping-spring systems with two degrees of freedom (2DOF) motion are considered, as shown in Fig. 2. D_1 and D_2 are the diameters of the upstream and downstream cylinders, respectively. $G = 4D_2$ is the wall spacing between the upstream and downstream cylinders.

The first system (system 1) contains two elastically mounted cylinders of unequal diameters experiencing flow in the IL direction [Fig. 2(a)]. The second system (system 2) contains one larger stationary upstream cylinder and one elastically mounted downstream cylinder experiencing the flow in the IL direction [Fig. 2(b)].

The governing equations of the mass-damping-spring system are as follows:

$$m \frac{\partial^2 X_i(t)}{\partial t^2} + c \frac{\partial X_i(t)}{\partial t} + kX_i(t) = F_i(t), \tag{3}$$

where $i, j = 1, 2$; X_1 and X_2 denote the IL and CF directions, respectively; k is the spring stiffness. The natural frequencies in both the IL and CF directions are tuned to the same value, resulting in equal stiffness in both directions. m is the structural mass. $F_1(F_x)$ and $F_2(F_y)$ are the fluid forces acting in the IL and CF directions, respectively. The temporal integration of the dynamic equations is performed numerically using the Newmark- β algorithm. The arbitrary Lagrangian–Eulerian (ALE) approach is applied in OpenFOAM for a dynamic mesh.

C. Physical parameters, computational domain, and boundary conditions

A summary of the parameters used in the simulations is presented in Table I. The parameters are obtained from an experiment of flexible cylinders.²⁹ The inlet velocity ranges from 0.04 to 0.14 at 0.01 intervals (m/s). The corresponding reduced velocity Vr_1 ranges from 3.13 to 10.97 at 0.78 intervals, and Vr_2 ranges from 4.45 to 15.58 at 1.11 intervals. The natural frequency of the elastically mounted bluff cylinder is close to the first-order frequency of the cylinder.

The mass ratio, natural frequency, damping ratio, and reduced velocity are expressed as the following:

TABLE I. Physical properties of the cylinders.

Parameter	System 1		System 2	
	Upstream cylinder	Downstream cylinder	Upstream cylinder	Downstream cylinder
Diameter (m)	$D_1 = 0.028\ 23$	$D_2 = 0.018\ 05$	$D_1 = 0.028\ 23$	$D_2 = 0.018\ 05$
Mass ratio	$m_1^* = 2.69$	$m_2^* = 2.00$...	$m_2^* = 2.00$
Natural frequency (Hz)	$f_{n1} = 0.45$	$f_{n1} = 0.50$...	$f_{n1} = 0.50$
Reduced velocity	$Vr_1 = 3.13\text{--}10.97$	$Vr_2 = 4.45\text{--}15.58$...	$Vr_2 = 4.45\text{--}15.58$
Inlet velocity (m/s)	$V = [0.04 : 0.01 : 0.14]$		$V = [0.04 : 0.01 : 0.14]$	

$$m^* = \frac{m}{m_w}, \quad f_n = 2\pi\sqrt{\frac{k}{m}}, \quad Vr_i = \frac{V}{f_n D_i}, \quad (4)$$

where m_w is the mass of the displaced fluid ($\rho = 1000 \text{ kg/m}^3$).

The drag coefficient C_D and lift coefficient C_L are defined as follows:

$$C_D = \frac{F_D}{\rho V^2 D/2}, \quad (5)$$

$$C_L = \frac{F_L}{\rho V^2 D/2}, \quad (6)$$

where F_D and F_L are the total unit drag and lift forces on the cylinder and $\rho = 1000 \text{ kg/m}^3$ is the density of the fluid.

The computational domain is $34D_2 \times 20D_2$ for two cylinders and is large enough to eliminate boundary effects, which are similar to Ref. 28. As shown in Fig. 3, the origin of the coordinate is located at the center of the upstream cylinder. The entire domain includes six boundaries. The farthest distance between the flow inlet boundary and the upstream cylinder is set as $10D_2$, and the farthest distance between the flow outlet boundary and the downstream cylinder is set as $20D_2$. The distance between the walls of the two cylinders is set as $4D_2$. The top and bottom symmetry boundaries are located at a distance of $10D_2$ from the center of the cylinder.

The boundary conditions used for the simulations are set as follows:

1. A uniform flow, $u_1 = V, u_2 = 0$, is set at the inlet boundary; the pressure p is specified as a zero normal gradient at the inlet boundary. Moreover, k and ω at the inlet boundary are calculated as follows:³³

$$k = \frac{3}{2}(VI)^2, \quad \omega = \sqrt{k}/C_\mu l, \quad (7)$$

where $C_\mu = 0.09$ is the empirical model constant, $I = 2\%$ is the turbulent intensity, and $l \approx 0.07D_1/C_\mu^{3/2}$ is the turbulent length scale.

2. Along the outlet boundary, u_1, u_2, k , and ω are set as zero gradients. The pressure p is set as $p = 0$.

3. Symmetry boundary conditions (zero normal gradient conditions) are applied for u_1, u_2, p, k , and ω at the top and bottom symmetry boundaries.
4. On the surface of the cylinder walls, a no-slip boundary condition is prescribed: $u_1 = 0, u_2 = 0, k = 0$, and ω are calculated as follows:³⁴

$$\omega = \frac{60\nu}{\beta_1 \Delta y_1^2}, \quad (8)$$

where $\beta_1 = 0.075$ is the model constant and Δy_1 is the distance to the next point away from the cylinder surface. $y^+ < 1$ is guaranteed in the present study. The first wall distance Δy_1 is estimated as the following:

$$\Delta y_1 = \frac{y^+ V}{u_*}, \quad u_* = \sqrt{\frac{1}{2} C_f} V^2, \quad C_f = (2\lg(\text{Re}) - 0.65)^{-2.3}. \quad (9)$$

D. Method validation

The present method is applied to simulate the 2DOF VIV of a single bluff cylinder. The physical parameters are obtained from a previous experiment,^{1,35} as shown in Table II. The fluid domain size is $20D \times 40D$. A sketch of the fluid domain and mesh used for simulation is shown in Fig. 4. The inlet boundary condition is set as an accelerated velocity at a speed of 0.025 per nondimensional time (tV/D), and the other boundary conditions are the same as shown in Fig. 3. The spatial and temporal schemes are consistent with the simulation of tandem cylinders. The mesh has been evaluated for mesh independence.

Figure 5 shows the VIV response amplitudes of the isolated bluff cylinder in the CF (A_y/D) and IL (A_x/D) directions. The amplitude A_y/D is defined as the maximum dimensionless VIV amplitude calculated by $\sqrt{2}y_{rms}/D$, and the RMS value is calculated from at least twenty stable VIV periods. The frequency ratio f_y/f_{na} is defined as the ratio of the dominant response frequency and natural frequency in water ($C_m = 1.00$). The natural frequency in water using an added mass coefficient of unity agrees well with the experiment.³⁶ Jauvtis and Williamson¹ defined the evolutionary process of a 2DOF VIV with

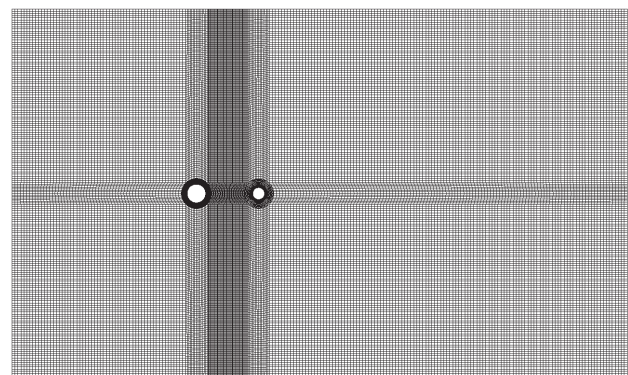
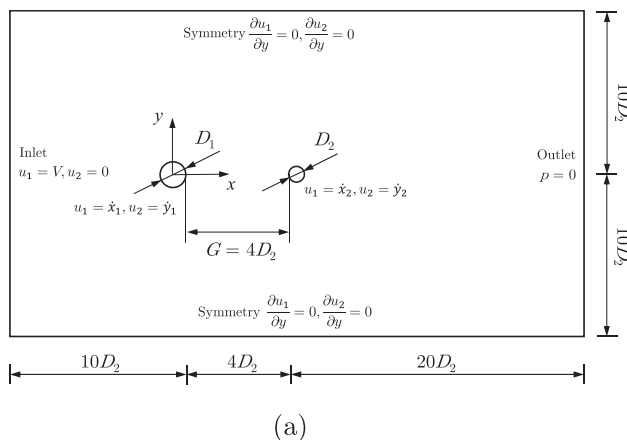


FIG. 3. Computational domain for the FIV of tandem cylinders: (a) sketch of the computational domain and (b) mesh of the fluid domain.

TABLE II. Physical properties of the isolated cylinder.

Parameter	Value for an isolated cylinder
Diameter D (m)	0.05
Mass ratio m^* (\dots)	2.60
Natural frequency in water (f_{na} , $C_m = 1.00$) (Hz)	0.45
Mass-damping ratio ($m^*\zeta + \zeta$) (\dots)	0.013
Flow velocity V (m/s)	0.06–0.30
Reduced velocity Vr (\dots)	3.00–15.00

$m^* = 2.6$, which primarily contains the initial branch ($4 < Vr < 6$), super upper branch ($6 < Vr < 8$), and lower branch ($Vr > 8$). The numerical simulation results are in great agreement with the experimental results. With increasing Vr , the maximum response reaches $1.5D$ at $Vr=8$ in the superupper branch and shifts to the lower branch with an amplitude less than $0.7D$ with a synchronized frequency ratio of approximately 1.30.

The numerical results agree well with the experimental data. The main three branches and maximum response amplitude are almost the same as the experimental value. The frequency ratios obtained from the simulations are also consistent with experimental observations, with a stable frequency ratio in the lower branch where the reduced velocity is greater than 8.00. Generally, the present approach seems to provide reasonable accuracy and performance in capturing the essential physics of VIV.

E. Mesh independency test

The mesh dependency test is conducted for the flow-induced vibration of two elastically mounted cylinders (system 1) of unequal diameters in tandem arrangement with $V = 1.00$ m/s with a rather high amplitude and contains a complicated dynamic mesh. Three different meshes TC1, TC2, and TC3 are employed for the test with different densities of the mesh around the cylinder, including the aspect ratio and the boundary layer mesh growth rate. $y^+ < 1.00$ is

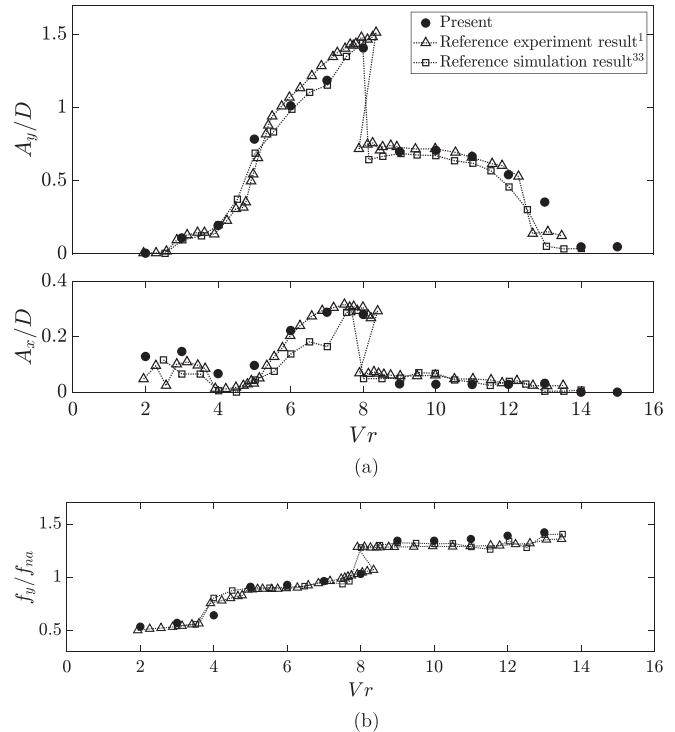
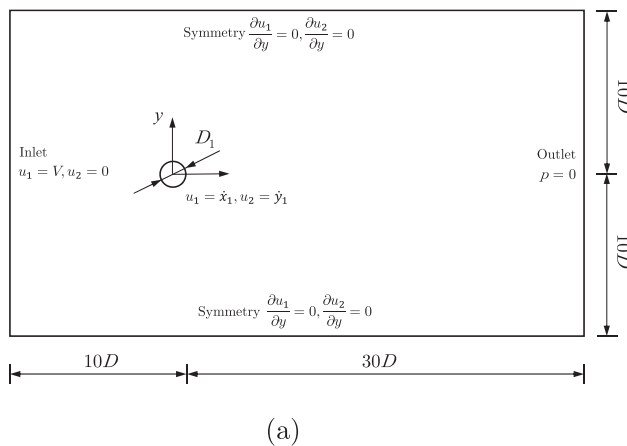


FIG. 5. VIV response amplitude (A_x/D and A_y/D) and CF frequency ratio (f_y/f_{na}) of the isolated cylinder. Black dots, present results; triangle frame, results from Ref. 1; and square frame, results from Ref. 35. (a) Response amplitude in the CF and IL directions, respectively, and (b) frequency ratio in the CF direction.

guaranteed in all test meshes. The maximum number of test meshes reached 58 376.

The time step Δt is set with Courant number $Co \leq 0.80$ for all cases to ensure time independence.³⁵ The Courant number Co (CFL condition) is defined as $Co = \frac{\Delta t}{2V} \sum_{\text{faces}} |\phi_i|$,³² where V is the cell volume, ϕ is the face volumetric flux, and \sum_{faces} is over all cell faces. The simulation results are compared in terms of the vibrating amplitude in

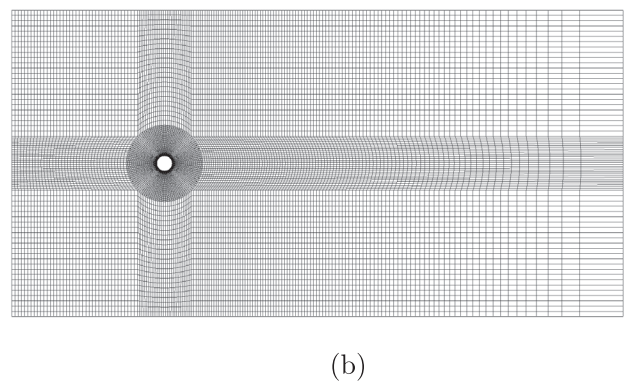


FIG. 4. Computational domain of the FIV of an isolated cylinder: (a) sketch of the computational domain and (b) mesh of the fluid domain.

TABLE III. Mesh dependency test for the flow-induced vibration of two elastically mounted cylinders.

Mesh description		Upstream cylinder					Downstream cylinder				
Case	Elements	A_{y1}/D_1	A_{x1}/D_1	\bar{C}_{D1}	C_{L1}^{max}	f_{y1}/f_{n1}	A_{y2}/D_2	A_{x2}/D_2	\bar{C}_{D2}	C_{L2}^{max}	f_{y2}/f_{n2}
TC1	46 716	0.57	0.03	1.23	0.37	1.36	1.41	0.50	1.49	1.11	1.24
TC2	50 591	0.59	0.03	1.23	0.34	1.33	1.44	0.51	1.56	1.08	1.21
TC3	58 376	0.62	0.03	1.24	0.32	1.31	1.42	0.47	1.52	1.02	1.19
Error rate (%)		3.39	0.00	0.00	8.82	2.26	2.08	1.96	4.49	2.78	2.48
		5.08	0.00	0.81	5.88	1.50	1.39	7.84	2.56	5.56	1.65

the IL and CF directions, and the mean drag coefficients, maximum lift coefficient, and frequency ratio in the CF direction are compared. For the error rate term, the first and second rows of values reflect the error values of TC1 and TC3 relative to TC2, respectively. We can see that the different meshes have little effect on the results, as shown in Table III. It is observed that the maximum deviation of the results is less than 8.00% when comparing TC2 with TC1 and TC3. It can be seen that the TC2 mesh provides a good balance of computational cost and accuracy. Therefore, all the following investigations are simulated based on mesh TC2.

F. Time-varying FIV force identification based on the forgetting factor least squares (FFLS) algorithm

To analyze the mechanism of the frequency capture phenomenon, a time-varying FIV force identification method based on the forgetting factor least squares (FFLS) algorithm³⁷ is applied.

A decomposition method of the total transverse force proposed by Sarpkaya³⁸ is introduced. Assuming the displacement $y = A_0 \sin(2\pi ft)$, the total lift force is $F_L = F_{total} = F_0 \sin(2\pi ft + \varphi)$. φ is the phase difference between the total lift force and displacement. The total force (F_{total}) can be decomposed into two parts: the exciting force (F_e) in phase with velocity and the added mass force (F_m) in phase with acceleration as follows:

$$F_{total}(t) = \underbrace{\frac{1}{2\sqrt{2}\dot{y}_{rms}} \rho DV^2 C_e(t) \dot{y}(t)}_{F_e} - \underbrace{\frac{\pi D^2}{4} \rho C_m(t) \ddot{y}(t)}_{F_m}, \quad (10)$$

where the C_e is the excitation coefficient, and C_m is the added mass coefficient. The diagram of the decomposition method is shown in Fig. 6. This decomposition method is widely used in current FIV prediction programs such as Shear7⁴ and VIVANA.⁵

As mentioned in a previous study,¹ the total transverse force F_{total} is decomposed into two parts: the total potential added mass force F_p and a vortex force component F_v . In fact, the potential added mass force and vortex force are the same as F_m and F_e in Eq. (10), respectively. The difference is that the force is normalized by $0.5\rho V^2 DL$ in the reference, and the velocity phase is excluded in the present study.

The total energy transfer from fluid dynamics to body motion over a vibration cycle in the CF direction is given as

$$E = \int_0^T F_{total}(t) \dot{y}(t) dt. \quad (11)$$

Combing with the force decomposition method, E can be expressed as

$$E = E_{ex} + E_m = \int_0^T F_e(t) \dot{y}(t) dt + \int_0^T F_m(t) \dot{y}(t) dt, \quad (12)$$

where E_{ex} is the energy transfer associated with the excitation force and E_m is the energy transfer associated with the added mass force. E_m is given as

$$E_m = \int_0^T F_m(t) \dot{y}(t) dt = - \int_0^T \frac{\pi D^2}{4} \rho C_m(t) \dot{y}(t) \ddot{y}(t) dt. \quad (13)$$

Assuming a VIV response with a single dominant frequency $y = A_0 \sin(2\pi ft)$, the E_m can be further expressed as

$$E_m = -(2\pi f)^3 A_0^2 \int_0^T \frac{\pi D^2}{4} \rho C_m(t) \sin(2\pi ft) \cos(2\pi ft) dt. \quad (14)$$

Due to the orthogonality of trigonometric functions, we can see that $E_m = 0$ in one vibration cycle. This conclusion holds true for multi-frequency responses as well. So the total energy transfer E is simply the energy transfer associated with the excitation force (excitation energy)

$$E = E_{ex} = \int_0^T F_e(t) \dot{y}(t) dt \quad (15)$$

and the excitation power (P_{ex}), describing the instantaneous energy transfer, is defined as

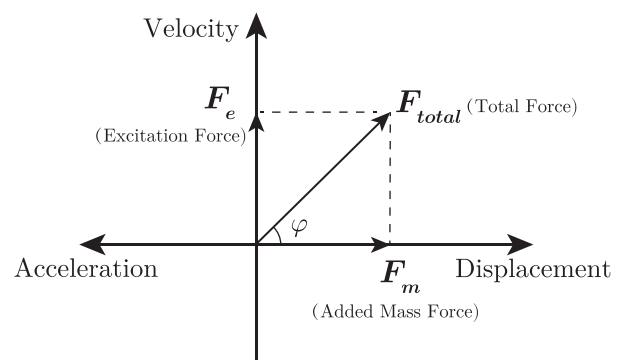


FIG. 6. Diagram of the force decomposition method. φ is the phase difference between the total lift force and the displacement.

$$P_{ex} = F_e(t)\dot{y}(t). \tag{16}$$

To investigate the fluid excitation mechanism, the exciting force F_e should be exacted from the total force F_{total} in the time domain. Jauvtis and Williamson¹ used the theoretical added force value, which is derived from the governing equation of vibration in the CF direction. This single-frequency theoretical model is valuable for evaluating the impact of physical parameters, but the FIV response typically contains a higher harmonic frequency component. Therefore, when dealing with real experimental data, this theoretical solution inevitably produces inaccuracy.

The forgetting factor least squares algorithm (FFLS)³⁷ is introduced here and used to calculate the exciting force F_e . Compared with the traditional least squares algorithm, the FFLS introduces a forgetting factor μ that divides the time history of the sampling data into different regions and assigns a greater weight to the data close to the present moment. This modification improves the sensitivity of the least squares method and makes it possible to identify the time-varying parameters. In addition, using previous historical moment data in vortex-induced force identification also respects the dynamic nature of both fluids and structures, and it may be possible to capture the memory effects. Equation (10) in the time domain can be rewritten as follows:

$$\begin{aligned} \mathbf{F}_s &= \mathbf{H}_s^* \boldsymbol{\theta}_s, \\ \mathbf{F}_s &= [F_{total}(t_1), F_{total}(t_2), F_{total}(t_3), \dots, F_{total}(t_s)]^T, \\ \mathbf{H}_s &= [\mathbf{h}(1), \mathbf{h}(2), \mathbf{h}(3), \dots, \mathbf{h}(s)]^T \\ &= \begin{bmatrix} \dot{y}(t_1), \dot{y}(t_2), \dot{y}(t_3), \dots, \dot{y}(t_s) \\ \ddot{y}(t_1), \ddot{y}(t_2), \ddot{y}(t_3), \dots, \ddot{y}(t_s) \end{bmatrix}^T, \\ \boldsymbol{\theta}(s) &= \begin{bmatrix} \frac{\rho DV^2}{2\sqrt{2}\dot{y}_{rms}} C_e(t_s) \\ -\frac{\rho \pi D^2}{4} C_m(t_s) \end{bmatrix}, \\ & s = 1, 2, 3, \dots \end{aligned} \tag{17}$$

In Eq. (17), the initial time step and the present time step are denoted as t_1 and t_s , respectively. $t_1, t_2, t_3, \dots, t_s$ represent the sampling time. \mathbf{F}_{total} is the time history of the total force. \mathbf{H}_s is the time history of velocity and acceleration from the initial time step t_1 to the present time step t_s . $\boldsymbol{\theta}_s$ is the force coefficient at t_s . Using only the data at the current moment cannot provide a unique solution for the estimation of the time-varying hydrodynamic coefficients. At a specific moment, there are two unknown variables [$C_e(t)$ and $C_m(t)$] in Eq. (10), but we only know one relation between these variables. This requires us to at least use a series of measurement data for the estimation, and an intuitive choice is using all data in previous measurements, such as the least square method.

The identification of time-varying flow-induced force can be treated as identifying the time history of $\boldsymbol{\theta}_s$. Equation (17) shows that all previous historical moments data before t_s are used to identify time-varying parameter $\boldsymbol{\theta}_s$. In the FFLS algorithm, the sampled force and response at different time steps are multiplied by different data weights β , and the data weight is larger if the data are closer to the present moment t_s . Specifically, the data weight of the present moment t_s is $\beta_0 = 1$, and the data weight of the initial moment is β^{s-1} , where

$\beta \in (0, 1]$. In the present study, β is set as a constant over time. Equation (17) can be rewritten as follows:

$$\begin{aligned} \mathbf{F}_s^* &= \mathbf{H}_s^* \boldsymbol{\theta}_s, \\ \mathbf{F}_s^* &= [\beta^{s-1} F_{total}(t_1), \beta^{s-2} F_{total}(t_2), \beta^{s-3} F_{total}(t_3), \dots, \beta^0 F_{total}(t_s)]^T, \\ \mathbf{H}_s^* &= [\beta^{s-1} \mathbf{h}(1), \beta^{s-2} \mathbf{h}(2), \beta^{s-3} \mathbf{h}(3), \dots, \beta^0 \mathbf{h}(s)]^T \\ &= \begin{bmatrix} \dot{y}(t_1), \dot{y}(t_2), \dot{y}(t_3), \dots, \dot{y}(t_s) \\ \ddot{y}(t_1), \ddot{y}(t_2), \ddot{y}(t_3), \dots, \ddot{y}(t_s) \end{bmatrix}^T, \\ \boldsymbol{\theta}(s) &= \begin{bmatrix} \frac{\rho DV^2}{2\sqrt{2}\dot{y}_{rms}} C_e(t_s) \\ -\frac{\rho \pi D^2}{4} C_m(t_s) \end{bmatrix}, \\ & s = 1, 2, 3, \dots \end{aligned} \tag{18}$$

In the FFLS algorithm, the parameters to be identified need to minimize the sum of the squared errors between $\mathbf{H}_s^* \boldsymbol{\theta}_s$ and \mathbf{F}_{total}^* as follows:

Then, we have the following:

$$\frac{\partial J(\boldsymbol{\theta})}{\partial \boldsymbol{\theta}} \Big|_{\hat{\boldsymbol{\theta}}_s} = \frac{\partial}{\partial \boldsymbol{\theta}} (\mathbf{F}_s^* - \mathbf{H}_s^* \boldsymbol{\theta}_s)^T (\mathbf{F}_s^* - \mathbf{H}_s^* \boldsymbol{\theta}_s) \Big|_{\hat{\boldsymbol{\theta}}_s} = \mathbf{0}. \tag{19}$$

After some matrix calculations, we can obtain

$$\hat{\boldsymbol{\theta}}_s = (\mathbf{H}_s^{*T} \mathbf{H}_s^*)^{-1} \mathbf{H}_s^{*T} \mathbf{F}_s^*. \tag{20}$$

Substituting Eqs. (18) into (20), we can finally obtain

$$\begin{aligned} \hat{\boldsymbol{\theta}}_s &= \left[\sum_{i=1}^s \beta^{2(s-i)} \mathbf{h}(i) \mathbf{h}^T(i) \right]^{-1} \left[\sum_{i=1}^s \beta^{2(s-i)} \mathbf{h}(i) F_{total}(i) \right] \\ &= \left[\sum_{i=1}^s \mu^{(s-i)} \mathbf{h}(i) \mathbf{h}^T(i) \right]^{-1} \left[\sum_{i=1}^s \mu^{(s-i)} \mathbf{h}(i) F_{total}(i) \right] \\ &= (\mathbf{H}_s^T \boldsymbol{\Lambda}_s \mathbf{H}_s)^{-1} \mathbf{H}_s^T \boldsymbol{\Lambda}_s \mathbf{F}_s, \end{aligned} \tag{21}$$

where $\mu = \beta^2$, $\mu \in (0, 1]$, μ is called the forgetting factor, and $\boldsymbol{\Lambda}_s$ is the weighted matrix, which is a diagonal matrix $\boldsymbol{\Lambda}_s = \text{diag}(\mu^{s-1}, \mu^{s-2}, \dots, \mu, 1)$. The essence of this method is to give different weights to the data: the farther away from the present moment of data is, the smaller the weight, as shown in Fig. 7.

This algorithm has been applied in the mechanical analysis of a bluff cylinder VIV in 2DOFs in the Appendix. The results match well with the experimental results¹ and can reflect the multifrequency characteristic. The mechanism of the frequency capture phenomenon is analyzed based on the FFLS algorithm in the following.

III. RESULTS AND DISCUSSION

A. Response amplitude

1. System 1

Figure 8 displays the IL and CF response amplitudes of system 1. The reduced velocity is based on the corresponding natural frequencies displayed in Table I. The black solid circles and squares represent the response of the upstream and downstream cylinder in system 1, respectively. The blue rhombuses represent the response amplitude of

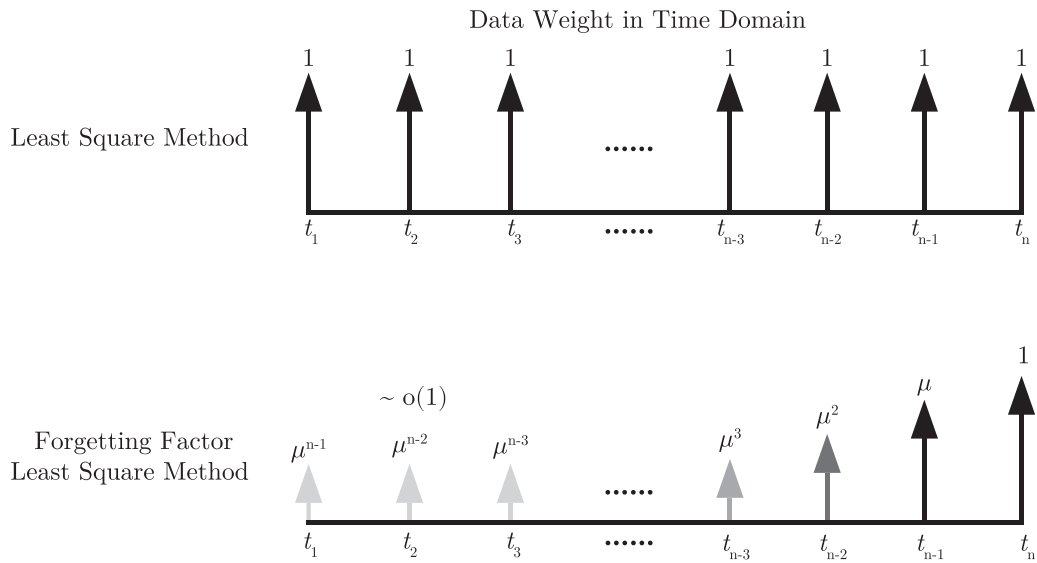


FIG. 7. Diagram of the data weight in the time domain for the FFLS algorithm.

the upstream cylinder of system 1 in Ref. 28 with different diameters under $V = 0.50$ m/s. The green stars represent the response amplitude of the downstream cylinder with the same system in Ref. 28. The purple circles represent the response amplitude of the upstream cylinder in system 1 with the same diameter in laminar flow $Re = 150$ in Ref. 39. The orange circles represent the corresponding results of the

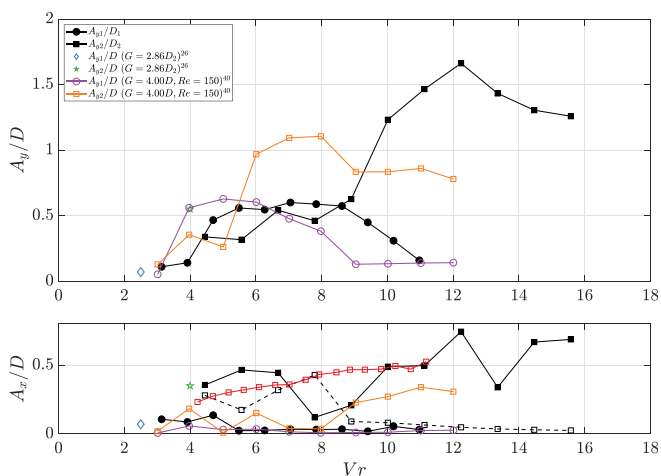


FIG. 8. Nondimensional FIV response amplitude of system 1 vs Vr . Top: response amplitude in the CF direction; bottom: response amplitude in the IL direction; black solid circles, response amplitude of the upstream cylinder of system 1; black solid squares, response amplitude of the downstream cylinder of system 1; blue rhombuses, response amplitude of the upstream cylinder of system 1 in Ref. 28; green stars, response amplitude of the downstream cylinder of system 1 in Ref. 28; purple circles, response amplitude of the upstream cylinder of system 1 with constant $Re = 150$ in Ref. 39; orange squares, response amplitude of the downstream cylinder of system 1 in Ref. 39. The subscript of the diameter is omitted in the reference results.

downstream cylinder in Ref. 39. The reference response amplitude is dimensionless by the corresponding diameter, and the subscripts of the diameters in the legend are omitted.

For the CF response, the vibration of the upstream cylinder in system 1 can be divided into three regimes: the increasing regime ($Vr < 4.00$), where the response grows with increasing velocity; the upper regime ($4.00 < Vr < 9.00$), where the response is relatively larger than other regimes; and the decreasing regime ($Vr > 9.00$), where the response decreases with increasing velocity. The upstream cylinder in system 1 reaches an approximate response amplitude $A_y \approx 0.60D$ compared with the laminar flow simulation. However, the upstream cylinder in laminar flow³⁹ reaches the maximum amplitude at a significantly lower reduced velocity ($Vr = 4.00$) compared with a higher Re simulation ($Vr = 5.50$). Compared with the isolated vibrating cylinder, the upstream cylinder in the present study contains no upper branch and reaches a lower amplitude compared with Fig. 5(a). The results of system 1 with different diameters in Ref. 28 are close to the numerical simulation results in this paper, which improves the credibility of the results of this paper.

The downstream cylinder response reflects a distinct WIV characteristic, with a greater response amplitude that does not decrease with increasing velocity. Two distinct regimes can be distinguished in the downstream cylinder vibration response of system 1: an increasing regime ($Vr < 12.00$) and a decreasing regime ($Vr > 12.00$). For the downstream cylinder, the response amplitude decreases at a lower reduced velocity than that of the upstream cylinder in the decreasing regime. The downstream cylinder in system 1 reaches its maximum amplitude of $1.66D$.

For the IL response, the vibration of the upstream cylinder is small and irregular vs Vr , which is also found in Refs. 28 and 39. There exists a switching $Vr \approx 8$. When $Vr > 8$, the response amplitude grows as the velocity increases, and the response amplitude result in the present study is higher than that in laminar flow.

2. System 2

Figure 9 shows the IL and CF response amplitudes of system 2. The black squares represent the response of the downstream cylinder in system 2. The red squares represent the response of the downstream cylinder of system 2 in Ref. 20. The reference response amplitude is dimensionless by the corresponding diameter, and the subscripts of the diameters in the legend are omitted.

For the CF response, the downstream cylinder in system 1 reaches a larger response amplitude (1.66D) than the downstream cylinder in system 2 (1.29D) and switches to the decreasing regime at a lower velocity, whereas the downstream cylinder in system 2 switches to the decreasing regime at $Vr = 10.00$. Compared with the simulation result of system 2 with the same diameters in Ref. 20, the increase in the response amplitude with reduced velocity follows a consistent pattern at $8.00 < Vr < 10.00$ and is slightly smaller at $Vr < 8.00$. The response of the downstream cylinder with the same and different diameters as system 2 displays a close response trend, but the maximum response amplitude and regimes shift to a reduced velocity are different. Further considering the effect of the Reynolds number,³⁹ the response amplitude of the downstream cylinder of system 2 in laminar flow still reaches a response over 1.00D, but the switch reduced velocity is smaller compared with a higher Re simulation.

For the IL response, the response of the downstream cylinder of system 1 reaches a higher response amplitude than that of system 2. There also exists a switch reduced velocity in system 2 at $Vr = 7.78$, but the response is more irregular vs Vr of system 1, which is also found in the laminar flow simulation.³⁹

B. Response frequency

Figure 10 demonstrates the trend of the response frequencies of the two systems vs the reduced velocity, where the reduced velocity is calculated from the corresponding natural frequencies shown in Table I. The black circles and squares represent the response

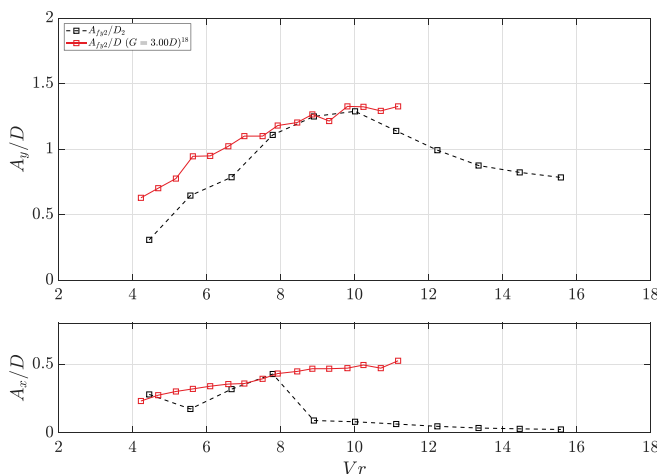


FIG. 9. Nondimensional FIV response amplitude vs Vr . Top: response amplitude in the CF direction; bottom: response amplitude in the IL direction; black squares, response amplitude of the downstream cylinder of system 2; red squares, response amplitude of the downstream cylinder of system 2 with same diameter in Ref. 20. The subscript of the diameter is omitted in the reference results.

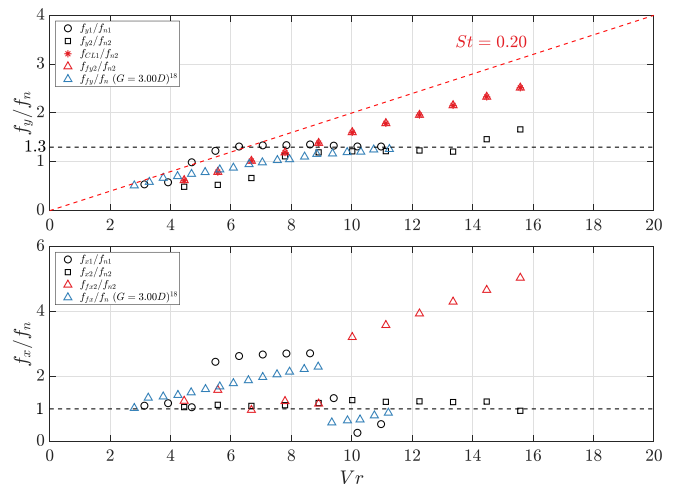


FIG. 10. Nondimensional FIV response frequency vs Vr . Top: response frequency in the CF direction; bottom: response frequency in the IL direction; black circles, response frequency of the upstream cylinder of system 1; black squares, response frequency of the downstream cylinder of system 1; red stars, dominant frequency of the lift force of the upstream cylinder of system 2; red triangles, response frequency of the downstream cylinder of system 2; blue triangles, response frequency of the downstream cylinder of system 2 with the same diameter as in Ref. 20.

frequencies of the upstream and downstream cylinders in system 1, respectively. The red stars represent the dominant frequency of the lift force of the downstream cylinder of system 2. The red triangles represent the response frequency of the downstream cylinder of system 2. The blue triangles represent the response frequency of the downstream cylinder of system 2 in Ref. 20.

For the CF response frequency, there exists a lock-in region when the reduced velocity is greater than 6.00 in the CF direction, with the nondimensional frequency value remains near 1.30 in the upstream cylinder in system 1. This is the same as the VIV of the isolated cylinder with $m^* \sim 2.00$ in Sec. II and previous study.¹ There also exists a lock-in region in the downstream cylinder in the CF direction that is slightly delayed compared to the upstream cylinder. Figure 11 shows the response frequencies in the CF direction of the upstream and downstream cylinders of system 1. It can be discovered that “frequency capture” exists under most simulation conditions. The vibration frequencies of the upstream and downstream cylinders are not equal in the preliminary lock-in and non-synchronization regions.

In system 2, the CF vibration frequencies are the same as the dominant frequency of the lift coefficient of the upstream cylinder in

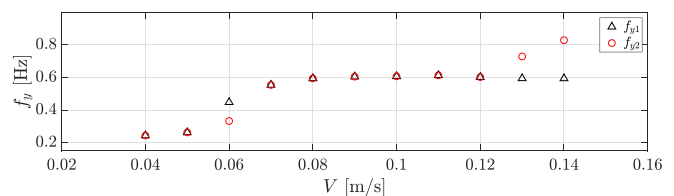


FIG. 11. FIV response frequency vs inlet velocity V in system 1 in the CF direction; black triangles, response frequency of the upstream cylinder of system 1; red circles, response frequency of the downstream cylinder of system 1.

all simulation conditions, which means that vortex shedding (the vortex shedding frequency of the stationary cylinder is equal to the dominant lift frequency) influences the external force distribution of the downstream cylinder and controls the dominant frequency of the fluid force of the downstream cylinder. The frequency capture exists in all simulation conditions, and the lock-in phenomenon disappears in the CF direction. The results in Ref. 20 also show a similar response frequency pattern; the response frequency shows a linear increase with the reduced velocity, and the lock-in phenomenon disappears. The frequency capture phenomenon was not studied in the reference.

For the response in the IL direction, the dominant response frequency is equal to twice the CF response frequency or near the dominant frequency, and this result was also found in a previous study.²⁰ The frequency capture phenomenon does not occur in the IL direction, which was also discovered in our previous experiment.²⁹

Furthermore, the spectrum analysis results of system 1 and system 2 are shown in Figs. 13 and 14, respectively. In a previous investigation of the VIV of a bluff cylinder with 2DOF vibration, it was found that vibration with a single frequency can induce a high-frequency force, as shown in Fig. 12.

There is a significant third harmonic component in the lift. The high-frequency lift component is also found in the present study. In system 1, it can be found that the response of the upstream cylinder also has a third harmonic response at a flow velocity of 0.04 m/s [Fig. 13(a)], and the downstream cylinder also has a second and third lift component at a flow rate of 0.12 m/s [Fig. 13(d)]. For the three cases in which the frequency capture phenomenon does not occur in the present study ($V = 0.06, 0.13,$ and 0.14 m/s), the response of the downstream cylinder exhibits a broadband spectral response and contains response components with the same frequency as the upstream cylinder lift at $V = 0.06$ m/s. The case of $V = 0.13$ m/s is similar to the case of $V = 0.06$ m/s. For the case of $V = 0.14$ m/s [Fig. 13(f)], there are two significant frequency components in the upstream

cylinder: the CF response dominant frequency $f_1 = 0.59$ Hz and the lift dominant frequency $f_2 = 0.83$ Hz. f_1 represents the response frequency in the lock-in region. When assuming $St = 0.18$, the vortex shedding frequency $f_{st} = St \cdot U/D = 0.89$ Hz is close to $f_2 = 0.83$ Hz. Therefore, f_2 denotes the fundamental vortex shedding frequency. The dominant response frequency of the downstream cylinder f_2 is the fundamental vortex shedding frequency of the upstream cylinder. The downstream cylinder frequency is still equal to the upstream cylinder vortex shedding frequency, and the frequency capture phenomenon still occurs. However, since the upstream cylinder is locked, the two dominant frequencies are different. The vortex shedding frequency component of the upstream cylinder exists in the response of the downstream cylinder. This phenomenon is more distinct in system 2, as shown in Fig. 14. The vibration frequency of the downstream cylinder is captured by the upstream vortex shedding frequency. This is an important parameter for the investigation of the FIV prediction method⁴⁰ for multi-pipe systems.

C. Excitation mechanics of the frequency capture phenomenon

1. Excitation mechanics of system 1

This section shows the response and flow fields of the FIV development progress to better understand the mechanisms of the frequency capture phenomenon. Figure 15 shows the instantaneous vorticity contours for selected time steps of system 1 at $V = 0.08$ m/s. The time history of the FIV response and lift coefficients, as well as the results of the time-frequency analysis, is shown in the upper half of the figure. The wavelet transform based on the Morlet wavelet is applied for the time-frequency analysis. It should be noted that the time history of Fig. 15 does not include the stable FIV phase. The instantaneous fields of ω_z are displayed in the lower part of the figure. A shift in the FIV development phase flow pattern¹⁷ can be observed. At the

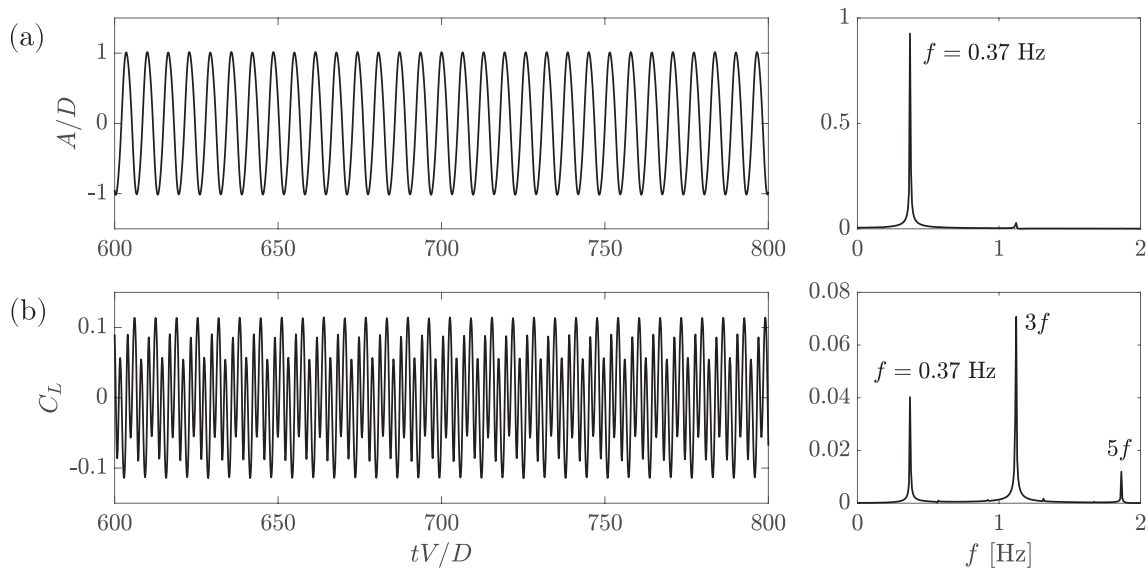


FIG. 12. Time history and frequency spectrum of VIV of the isolated cylinder in Sec. II D under $Vr = 6$: (a) time history of response the amplitude in the CF direction (left) and frequency spectrum by FFT (right) and (b) time history of the lift coefficient (left) and frequency spectrum by FFT (right).

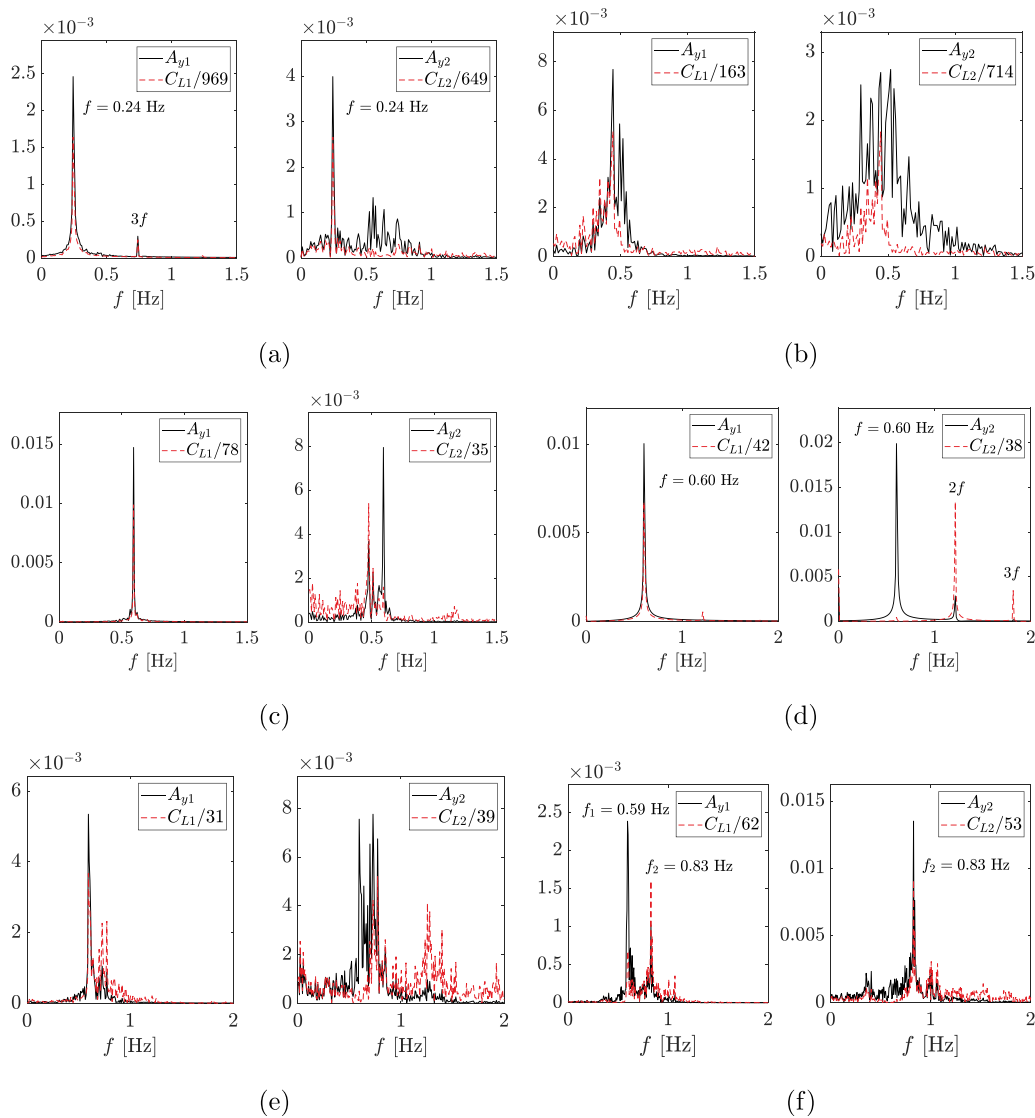


FIG. 13. Frequency spectrum of FIV in system 1 under the selected flow velocity: (a) $V = 0.04$, (b) $V = 0.06$, (c) $V = 0.08$, (d) $V = 0.12$, (e) $V = 0.13$, and (f) $V = 0.14$ m/s. Left: CF amplitude (black line) and lift force coefficient (red line) of the upstream cylinder; right: CF amplitude (black line) and lift force coefficient (red line) of the downstream cylinder.

beginning of the simulation, the wake vortex of the upstream cylinder has not yet formed, and the vortices have shifted from the downstream cylinder. The reattachment regime is established. Furthermore, the flow pattern switches from the reattachment regime to the co-shedding regime with the generation of the upstream vortex street, and this result has been found in all simulations in this paper. The spacing of the upstream and downstream cylinders is a key parameter of this phenomenon, and more studies with different spacings are planned. According to the wavelet analysis results, the response of the upstream cylinder contains a steady fundamental component, whereas the downstream cylinder is more unstable and contains the third harmonic component. The results of the lift coefficient are similar to the response, but the third harmonic component is more prominent.

Concerning the frequency capture phenomenon, the wavelet analysis shows that the downstream cylinder response frequency is not always equal to the upstream cylinder. The response of the downstream cylinder contains a considerable fundamental frequency component until 40 s, and the major frequency component of the response is consistent with the lift. As shown in Figs. 15(b)–15(d), the wake of the upstream cylinder intermittently hits the downstream cylinder, which results in an external excitation force with the fundamental frequency of the upstream cylinder. The wake formed by the upstream cylinder is larger than that of the downstream cylinder and changes the pressure distribution, which results in the frequency capture phenomenon.

Furthermore, we apply the FFLS algorithm to obtain the excitation force in the time domain. The energy transfer is evaluated by

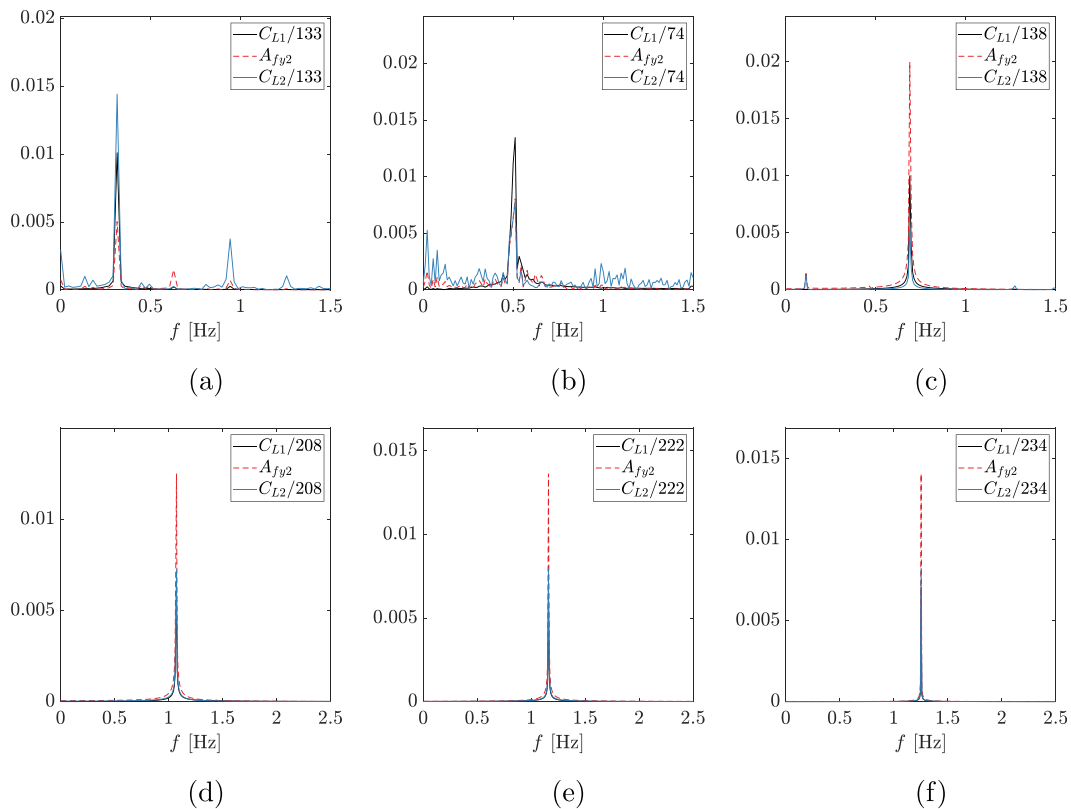


FIG. 14. FIV frequency spectrum in system 2 under selected flow velocities: (a) $V = 0.04$ m/s, (b) $V = 0.06$ m/s, (c) $V = 0.08$ m/s, (d) $V = 0.12$ m/s, (e) $V = 0.13$ m/s, and (f) $V = 0.14$ m/s. Black line, lift force coefficient of the upstream cylinder; red dashed line, CF amplitude of the downstream cylinder; blue line, lift force coefficient of the downstream cylinder.

excitation power $P_{ex} = F_{ex} \cdot \dot{A}_y$. The energy transfer of system 1 at $V = 0.08$ m/s is shown in Fig. 16. The energy transfer of the upstream cylinder is close to that of the isolated cylinder FIV, which is periodic and stable in the time domain. The energy transfer of the downstream cylinder is more chaotic and is strongly related to the occurrence of the frequency capture phenomenon. The power of the fluid is greater when the frequency capture phenomenon occurs, and the power reaches a relatively high value when the wake of the upstream cylinder exceeds that of the downstream cylinder.

Figure 17 shows the flow field at $V = 0.13$ m/s of system 1. The flow field also displays a transition from the reattachment regime to the co-shedding regime, similar to the 0.08 m/s simulation condition. Different from the result of $V = 0.08$ m/s, there exists a peak near 5 s in the wavelet analysis results. As shown in Fig. 17(b), a relatively large vortex formed during the FIV development phase, resulting in a relatively high lift and a peak value in the wavelet analysis. As discussed in Sec. III B, the frequency capture phenomenon does not occur in this simulation condition, and the downstream cylinder shows a broadband spectral response containing a response component with the same frequency as the upstream cylinder response. In addition, the wavelet analysis reveals that there exists competition in the dominant frequency of the downstream cylinder response and lift in the time domain.

The energy transfer of system 1 at $V = 0.13$ m/s is shown in Fig. 18. For the upstream cylinder, the large standing vortex near 5 s induces a high energy transfer. After the FIV reaches a state of equilibrium, the energy transfer tends to be periodic. For the downstream cylinder, there exist two regions of excitation power: $t < 25$ s and > 25 s. A high-frequency energy transfer is established at $t < 25$ s under the effect of the incoming flow and upstream cylinder wake. When the stable FIV is established, the energy transfer becomes periodic but contains more multifrequency components compared with the upstream cylinder.

Figure 19 represents the instantaneous vorticity contour under the stable FIV of system 1. The wake of the upstream cylinder does not hit the downstream cylinder in one period; therefore, the flow field contains both upstream and downstream cylinder wakes. However, since the downstream cylinder usually shows a broadband spectral response, its motion phase is unstable and will interact with the upstream cylinder wake at certain times, which makes the flow pattern more irregular.

2. Excitation mechanics of system 2

As shown in Fig. 20, system 2 appears to have a more consistent response, with the downstream cylinder response frequency being

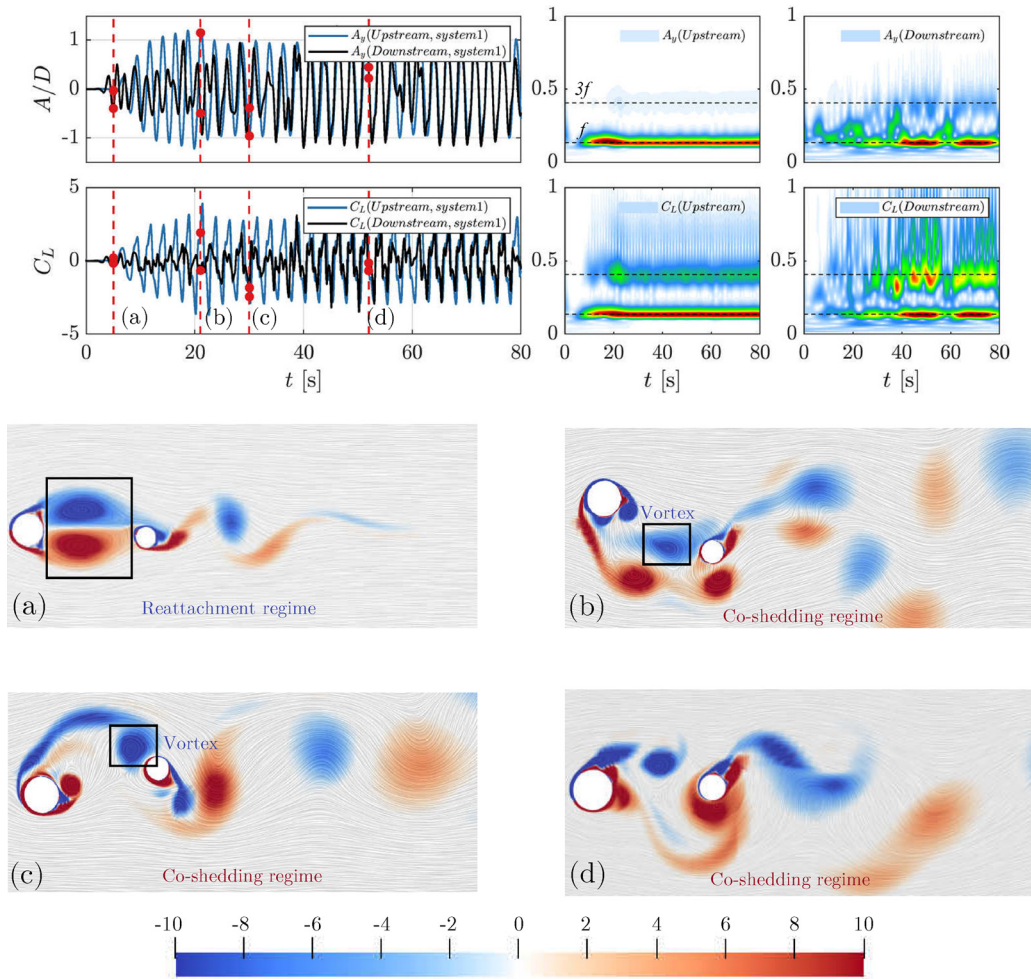


FIG. 15. Instantaneous vorticity contour for the wake pattern behind the two cylinders of selected time steps at $V = 0.08$ m/s of system 1: (a) $t = 5.00$, (b) $t = 21.00$, (c) $t = 30.00$, and (d) $t = 52.00$ s. Top: time history of the FIV response of upstream and downstream cylinders (left) and time-varying VIV response frequency of the cylinders (right). The red dashed lines represent selected time steps, and black dashed lines represent the dominant response frequency and third harmonic frequency; middle: time history and time-varying frequency of the lift coefficients of the upstream and downstream cylinders; bottom: instantaneous vorticity (ω_z) contour for the wake pattern behind the two cylinders of the selected time steps: blue represents a negative value, and red represents a positive value.

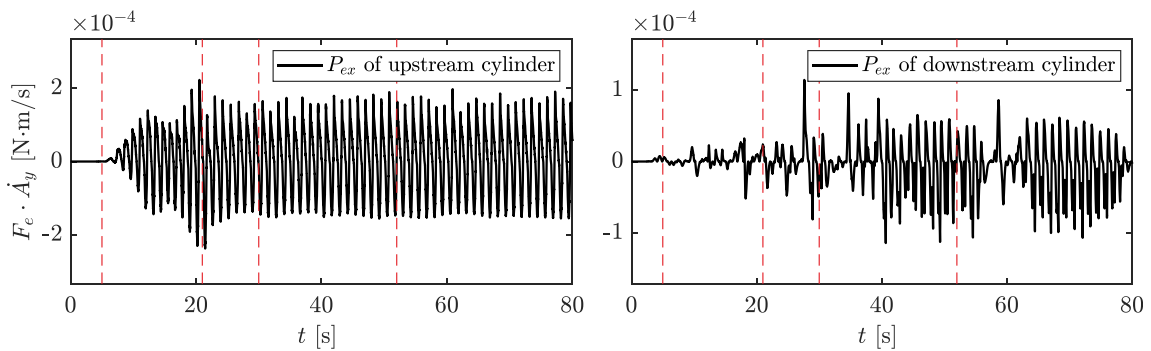


FIG. 16. Energy transfer due to the vorticity dynamics of system 1 at $V = 0.08$ m/s.

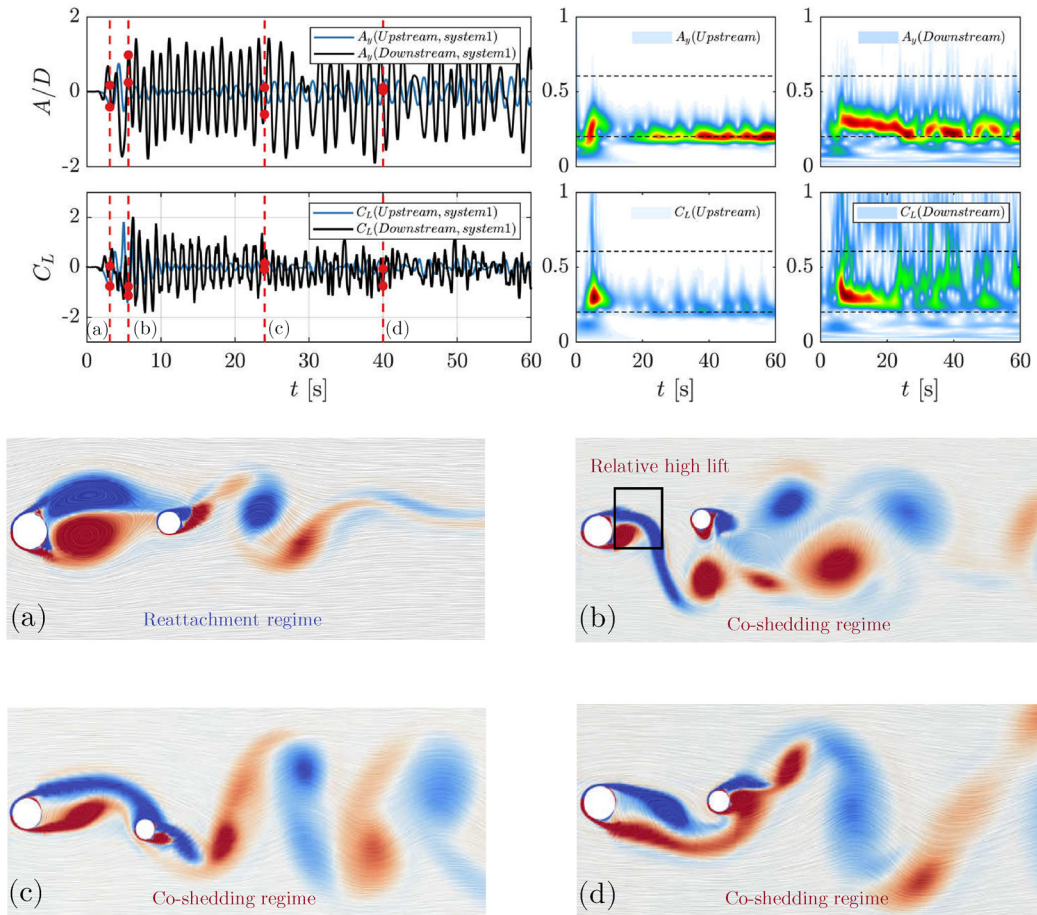


FIG. 17. Instantaneous vorticity contour for the wake pattern behind the two cylinders of selected time steps at $V = 0.13$ m/s of system 1: (a) $t = 3.10$, (b) $t = 5.60$, (c) $t = 24.00$, and (d) $t = 40.00$ s.

narrow-band and nearly constant with time. There also exists a transition from the reattachment regime to the co-shedding regime in system 2 with 2P flow pattern [Fig. 20(d)]. The downstream cylinder response stabilizes at the dominant frequency later than the upstream

lift coefficient, indicating that the downstream cylinder response is excited by the upstream wake and that the downstream tube lift has a more obvious higher harmonic frequency component induced by the 2P mode.

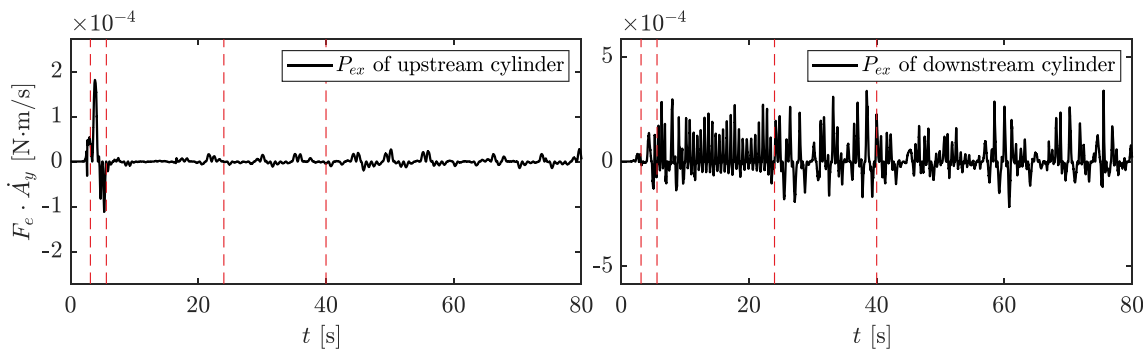


FIG. 18. Energy transfer due to the vorticity dynamics of system 1 at $V = 0.13$ m/s.

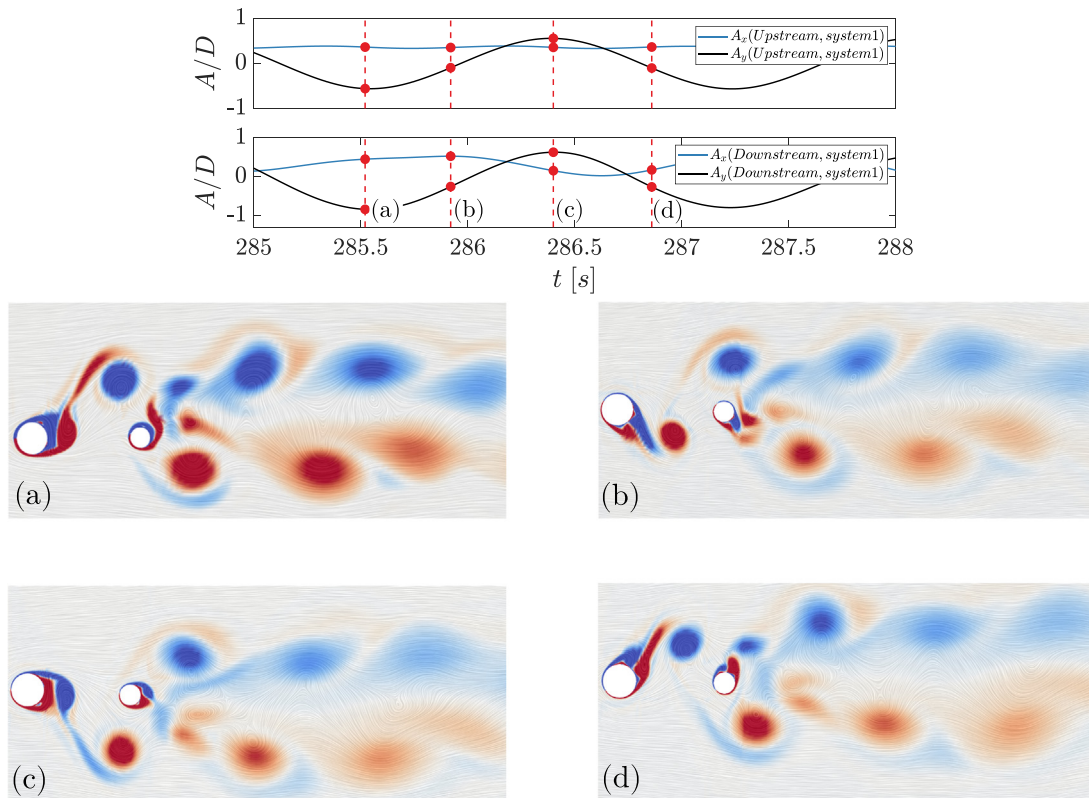


FIG. 19. Instantaneous vorticity contour behind the two cylinders at selected time steps with stable FIV at $V = 0.08$ m/s of system 1: (a) $t = 258.52$, (b) $t = 285.92$, (c) $t = 286.40$, and (d) $t = 286.86$ s. Top: time history of the FIV response of upstream and downstream cylinders. The red dashed lines represent selected time steps; middle: time history of the lift coefficients of the upstream and downstream cylinders; bottom: instantaneous vorticity (ω_2) contour for the wake pattern behind the two cylinders at selected time steps: blue represents a negative value, and red represents a positive value.

The energy transfer of system 2 at $V = 0.08$ m/s is shown in Fig. 21. The downstream cylinder of system 2 is dominated by the incoming flow when $t < 20$ s, where the power is periodic and similar to the FIV of the isolated cylinder. When the wake of the upstream cylinder begins hitting the downstream cylinder ($t > 20$ s), the power always remains positive, which means that the vorticity keeps the transfer energy to the downstream cylinder vibration system. This is clearer than in system 1, which shows the mechanism by which the frequency phenomenon occurs.

Figure 22 also indicates the transition from the reattachment regime to the co-shedding regime. As the flow rate increases, the standing vortex becomes larger and completely covers the downstream cylinder [Fig. 17(a)]. Similar to the condition where $V = 0.08$ m/s, the downstream is affected by the wake of the upstream cylinder after the wake forms [Figs. 17(b) and 17(c)]. However, the 2P mode does not occur in this simulated setting; instead, a 2S flow pattern with a small higher harmonic component forms behind the downstream cylinder.

The energy transfer of system 2 at $V = 0.13$ m/s is displayed in Fig. 23. Consistent with the condition of 0.08 m/s, the wake of the upstream cylinder always does positive work on the structure,

which means that there is energy transfer from the vorticity to the structure.

Figure 24 represents the instantaneous vorticity contour under stable FIV of system 2. Compared to system 1, a stable flow pattern is formed in system 2 due to the stationary upstream cylinder. As shown in Fig. 24, the vortex of the upstream cylinder is large enough to cover the downstream cylinder, which makes the flow field dominated by the wake of the upstream cylinder. In one FIV cycle, vortex 1 generated by the upstream cylinder [Fig. 19(a)] moves to the downstream cylinder and replaces the wake of the downstream cylinder [Figs. 19(b) and 19(c)] and further becomes the wake of the downstream cylinder [Fig. 19(d)]. Vortex 2 then also replaces the wake of the downstream cylinder, similar to vortex 1. Due to the vibration of the downstream cylinder, the 2S mode wake behind the upstream cylinder is converted to the 2P mode after passing through the downstream cylinder.

D. Trajectory

Figures 25 and 26 show the trajectories of the upstream and downstream cylinders of the different systems under selected flow conditions. It is discovered that the trajectory of the upstream cylinder in

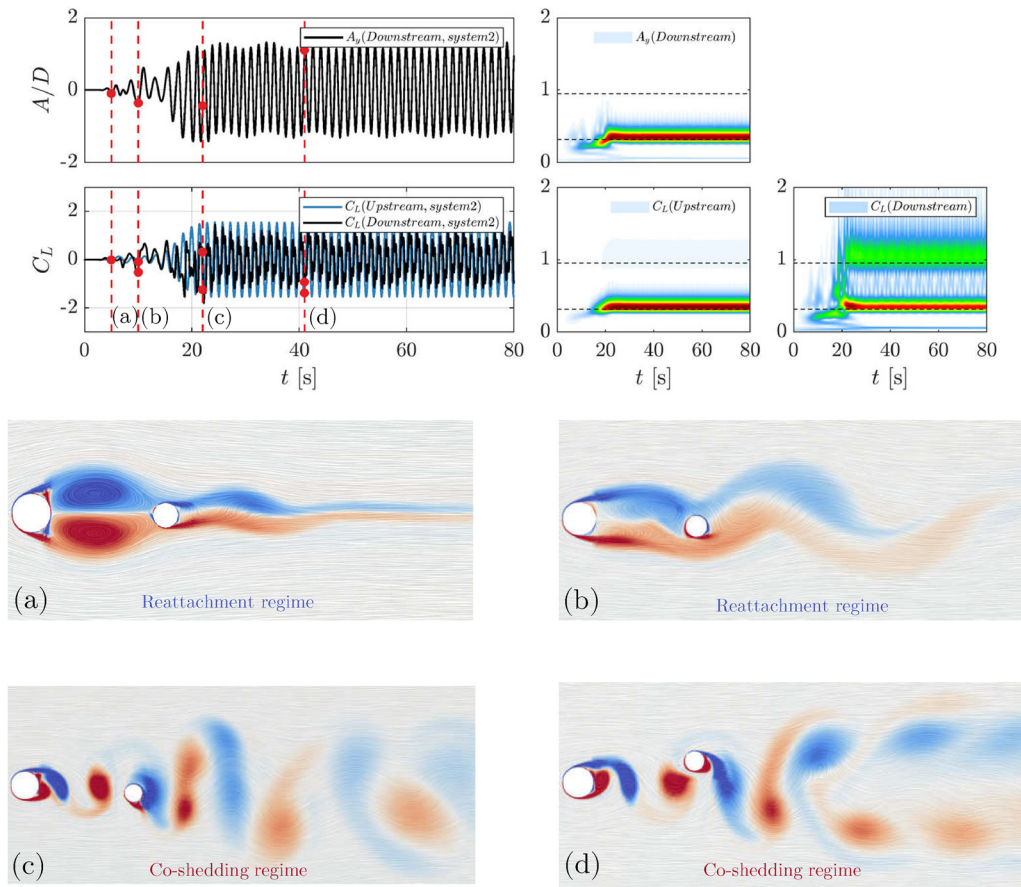


FIG. 20. Instantaneous vorticity contour for the wake pattern behind the two cylinders at selected time steps at $V = 0.08$ m/s in system 2: (a) $t = 5.00$, (b) $t = 10.00$, (c) $t = 22.00$, and (d) $t = 41.00$ s. Top: time history of the FIV response of the downstream cylinders (left) and the time-varying VIV response frequency of the downstream cylinder (right). The red dashed lines represent selected time steps, and black dashed lines represent the dominant frequency and third harmonic frequency; middle: time history and time-varying frequency of the lift coefficients of the upstream and downstream cylinders; bottom: instantaneous vorticity (ω_z) contour for the wake pattern behind the two cylinders at selected time steps: blue represents a negative value, and red represents a positive value.

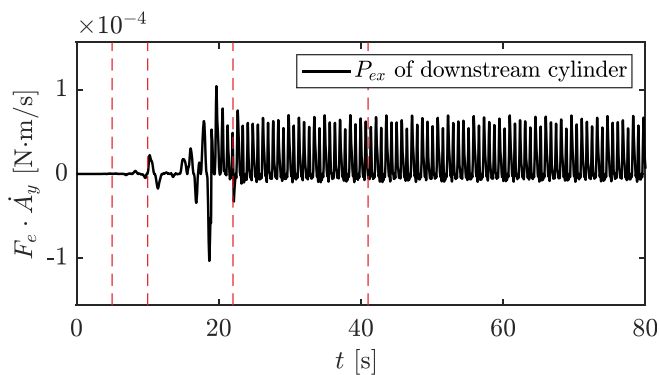


FIG. 21. Energy transfer due to vorticity dynamics of system 2 at $V = 0.08$ m/s.

system 1 is more stable than that of the downstream cylinder, which is also found in Ref. 28. The reason for this phenomenon is that the broadband spectral response of the downstream cylinder makes the phase more unstable with time. Compared with system 1, the trajectories of the downstream cylinder are more stable in system 2, which can also be found in the spectrum analysis that the downstream cylinder represents a narrow band spectrum response. The trajectories of the upstream cylinder show a figure-of-eight distribution, which is consistent with previous observations.

IV. SUMMARY

Flow-induced vibrations of two cylinders with different diameters in the tandem arrangement are investigated numerically. The distance between the walls of the two cylinders is set as $4D_2$. Two kinds of vibration systems with stationary and vibrating upstream cylinders are

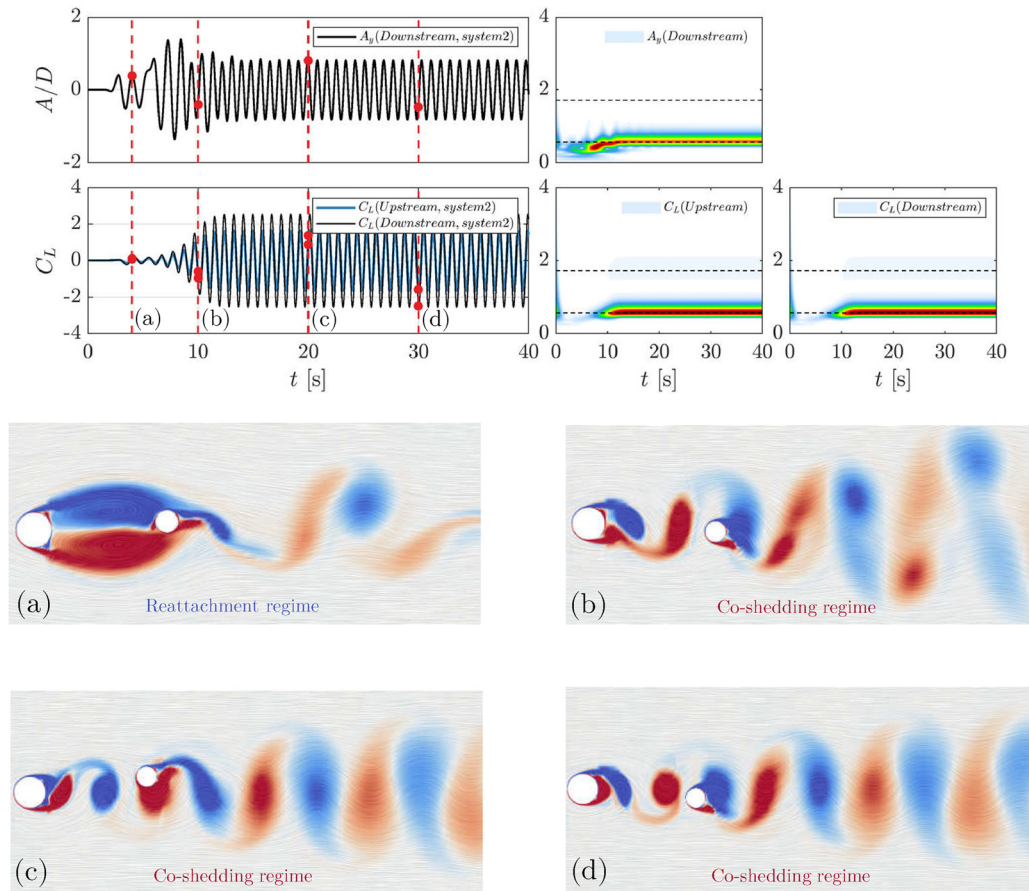


FIG. 22. Instantaneous vorticity contour for the wake pattern behind the two cylinders at selected time steps at $V = 0.13$ m/s in system 2: (a) $t = 4.00$, (b) $t = 10.00$, (c) $t = 20.00$, and (d) $t = 30.00$ s.

simulated. The reduced velocity of the downstream cylinder ranges from 4.45 to 15.58. The 2D computational model is developed to simulate the fluid–structure interaction, and this method is verified through VIV of an isolated cylinder in 2DOFs. The following conclusions may be drawn:

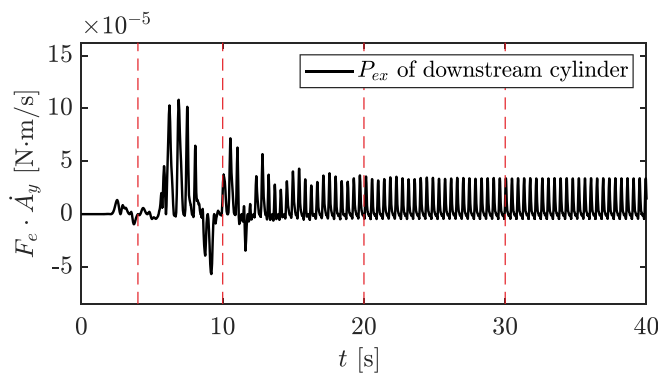


FIG. 23. Energy transfer due to vorticity dynamics of system 2 at $V = 0.13$ m/s.

1. The results for two kinds of systems are presented. The amplitude results show that the response of the downstream pipe is larger than that of the upstream cylinder, and the maximum amplitude in this paper surpasses $1.5D_2$.
2. Based on the frequency spectrum and flow pattern analysis, it is confirmed that the frequency capture phenomenon is caused by upstream vortex shedding, which makes the downstream external excitation frequency equal to the upstream vortex shedding frequency. Even if frequency capture does not occur, there is still a large upstream vortex shedding frequency component in the downstream cylinder response, which will be applied as a frequency model using the multicylinder FIV prediction method.
3. The excitation mechanism of the frequency capture phenomenon is investigated by the FFLS algorithm. The energy transfer due to the frequency capture phenomenon is always from vorticity to structure, which is quite different from the isolated cylinder VIV. This confirms that the phenomenon is induced by the interaction between the upstream cylinder wake and the downstream cylinder.

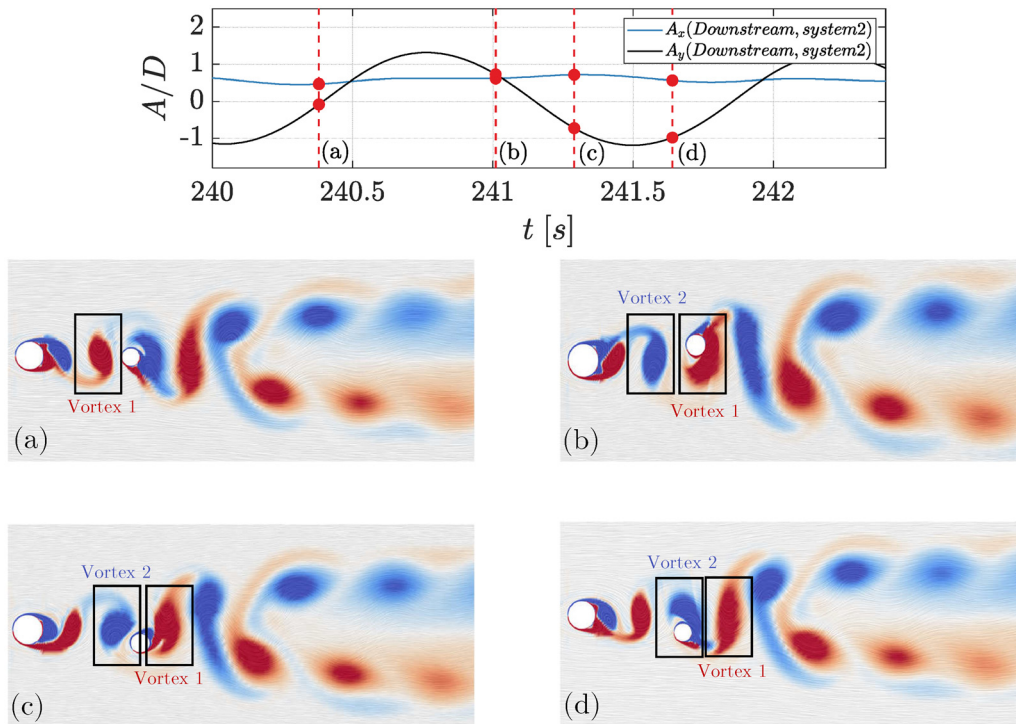


FIG. 24. Instantaneous vorticity contour behind the two cylinders at selected time steps with stable FIV at $V = 0.08$ m/s in system 2: (a) $t = 240.38$, (b) $t = 241.01$, (c) $t = 241.29$, and (d) $t = 241.64$ s. Top: time history of the FIV response of the downstream cylinder. The red dashed lines represent selected time steps; bottom: instantaneous vorticity (ω_z) contour for the wake pattern behind the two cylinders of selected time steps: blue represents negative value, and red represents positive value.

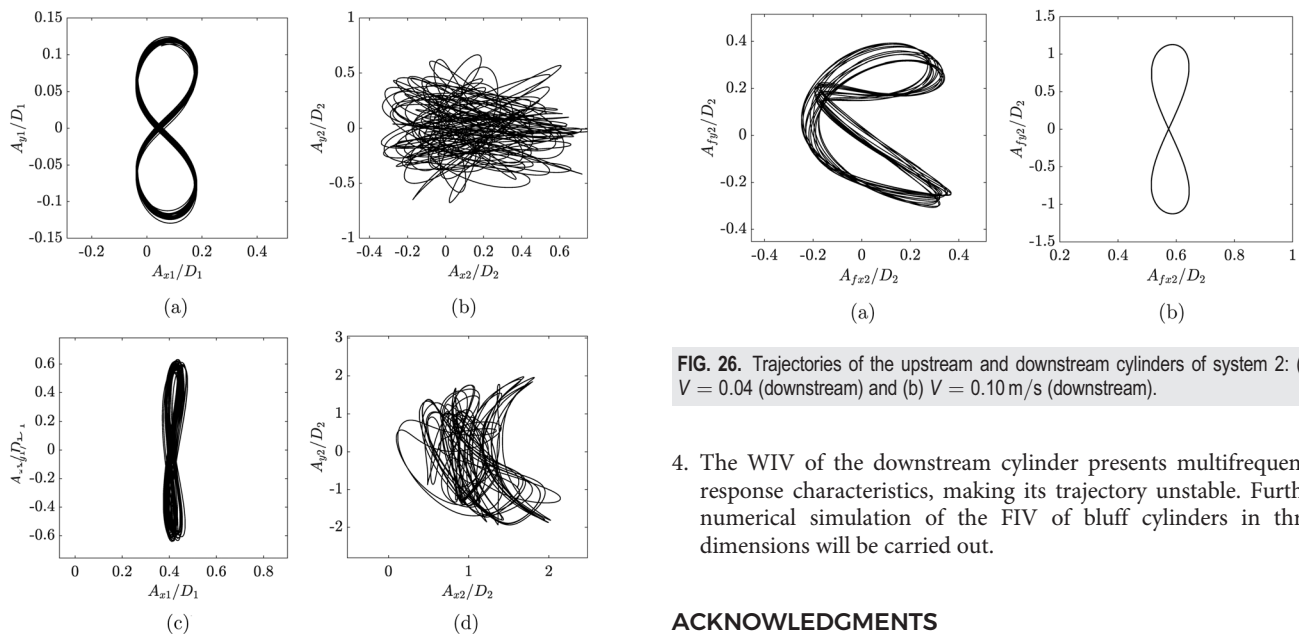


FIG. 25. Trajectories of the upstream and downstream cylinders of system 1: (a) $V = 0.04$ (upstream), (b) $V = 0.04$ (downstream), (c) $V = 0.10$ (upstream), and (d) $V = 0.12$ m/s (downstream).

FIG. 26. Trajectories of the upstream and downstream cylinders of system 2: (a) $V = 0.04$ (downstream) and (b) $V = 0.10$ m/s (downstream).

4. The WIV of the downstream cylinder presents multifrequency response characteristics, making its trajectory unstable. Further numerical simulation of the FIV of bluff cylinders in three dimensions will be carried out.

ACKNOWLEDGMENTS

The authors gratefully acknowledge the financial support from the National Natural Science Foundation of China under Grant No. 52088102; the Joint Funds of the National Natural Science

Foundation of China under Grant No. U19B2013; National Natural Science Foundation of China under Grant Nos. 52001208, 51909159, 52111530135; Shanghai Science and Technology Program under Grant Nos. 21ZR1434500, 19JC1412800, and 19JC1412801; Shenlan Project under Grant Nos. SL2020PT102 and SL2021MS018; Key projects for Intergovernmental Cooperation in International Science, Technology and Innovation under Grant No. 2018YFE0125100; National Science Fund for Distinguished Young Scholars under Grant No. 51825903; State Key Laboratory of Ocean Engineering (Shanghai Jiao Tong University) under Grant No. GKZD010081; and Chenguang Program supported by Shanghai Education Development Foundation and Shanghai Municipal Education Commission under Grant No. 21CGA15.

AUTHOR DECLARATIONS

Conflict of Interest

The authors have no conflicts to disclose.

Author Contributions

Xuepeng Fu: Writing – original draft (lead), Writing – review and editing (lead), Data curation (lead), Formal analysis (equal), and

Investigation (lead). **Shixiao Fu:** Conceptualization (equal), Funding acquisition (equal), and Supervision (equal). **Mengmeng Zhang:** Conceptualization (equal), Funding acquisition (equal), Investigation (equal), Supervision (equal), and Writing – review and editing (equal). **Zhaolong Han:** Data curation (equal), Methodology (equal), and Writing – review and editing (equal). **Haojie Ren:** Formal analysis (equal) and Investigation (equal). **Yuwang Xu:** Funding acquisition (equal) and Investigation (equal). **Bing Zhao:** Formal analysis (equal) and Investigation (supporting).

DATA AVAILABILITY

The data that support the findings of this study are available from the corresponding author upon reasonable request.

APPENDIX: ANALYSIS OF ISOLATED BLUFF CYLINDER VIV MECHANISMS WITH 2DOFs USING THE FFLS ALGORITHM

In this appendix, we first compared the least squares and forgetting factor least squares algorithm by identifying a self-defined multi-frequency vibration system. Then, we apply the FFLS algorithm to investigate the mechanism of the VIV of an isolated bluff cylinder. The parameters are displayed in Table II which is the same as Ref. 1.

A response signal with multi-frequency is assumed as

$$\begin{cases} y(t) = A_1 \sin(2\pi f_1 t + \varphi_1) + A_2 \sin(2\pi f_2 t + \varphi_2), \\ \dot{y}(t) = 2\pi f_1 A_1 \cos(2\pi f_1 t + \varphi_1) + 2\pi f_2 A_2 \cos(2\pi f_2 t + \varphi_2), \\ \ddot{y}(t) = -(2\pi f_1)^2 A_1 \sin(2\pi f_1 t + \varphi_1) - (2\pi f_2)^2 A_2 \sin(2\pi f_2 t + \varphi_2), \end{cases} \quad (A1)$$

where $A_1 = 0.01, A_2 = 0.005, f_1 = 1 \text{ Hz}, f_2 = 3f_1, \varphi_1 = \varphi_2 = 0$, and the force is calculated by the MCK equation

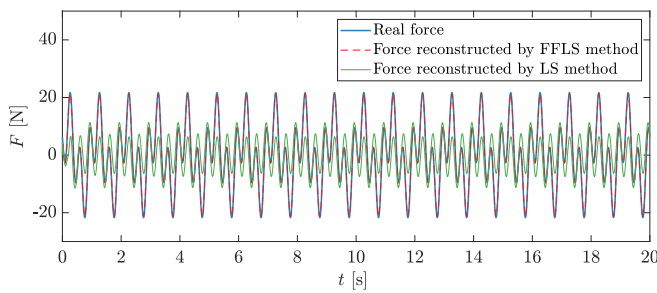


FIG. 27. Real force and reconstructed force by LS and FFLS methods.

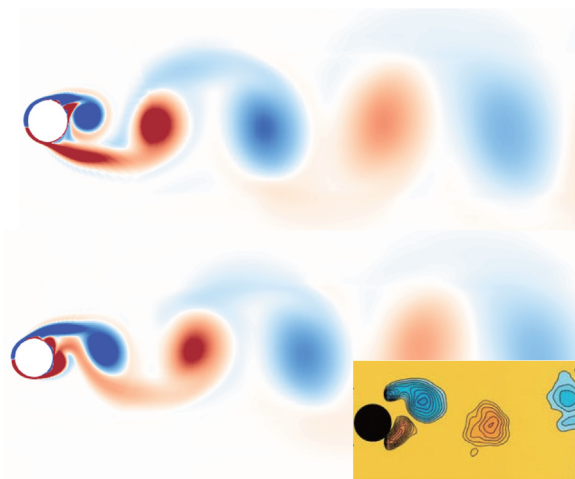
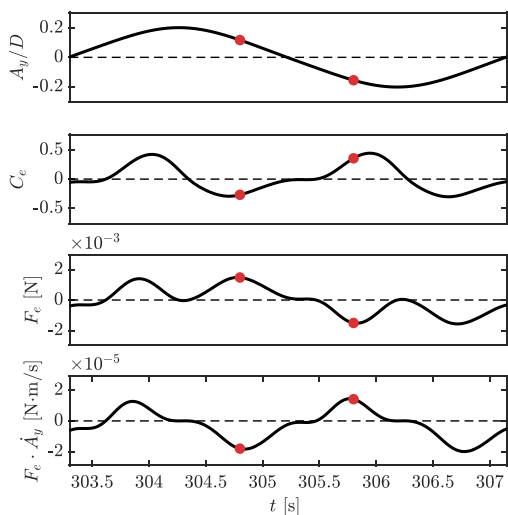


FIG. 28. Energy transfer due to vorticity dynamics for the 2S mode at $Vr = 4.00$. The parameters are the same as those in Ref. 1. Left: VIV response amplitude A_y/D , excitation coefficient C_e , excitation force F_e , and rate of energy transfer $F_e \cdot A_y$ (from top to bottom). Right: instantaneous vorticity contours correspond to the red symbols in the time profiles on the left. Vortex images with the yellow background are the results in Ref. 1.

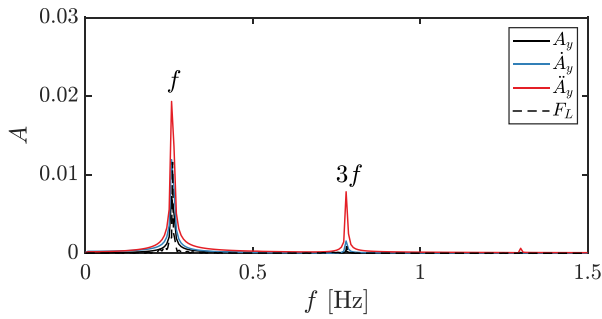


FIG. 29. FFT result of response amplitude, velocity, and acceleration.

$$My(t) + C\dot{y}(t) + K\ddot{y}(t) = F(t), \quad (A2)$$

where $M = 10, C = 40, K = 1500$.

Then, we can use the traditional LS (forgetting factor equal to 1) and FFLS method to identify the excitation and added mass coefficient. The reconstructed force by LS and FFLS methods is displayed in Fig. 27. The result shows that the FFLS method leads to more accurate reconstruction of multi-frequency force signals than LS method. And, the VIV response is widely known for multi-frequency force characteristic.⁴¹ Therefore, it is necessary to use the FFLS method to reconstruct the time-domain VIV force.

Jauvntis and Wiliiamson¹ introduced a significant qualitative rule that there exists a peak energy transfer into vertical motion when there is a dominance of clockwise vorticity moving downstream to the right as the body moves downward. This was also discovered in the present study, as shown in Fig. 28. $\omega_z = \partial v/\partial x - \partial u/\partial y$ is used for the instantaneous vorticity contours, and the positive (red) and negative (blue) values of ω_z represent anticlockwise and clockwise vorticity, respectively.

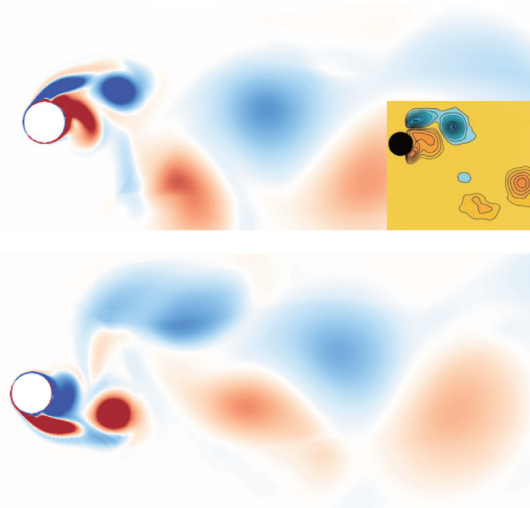
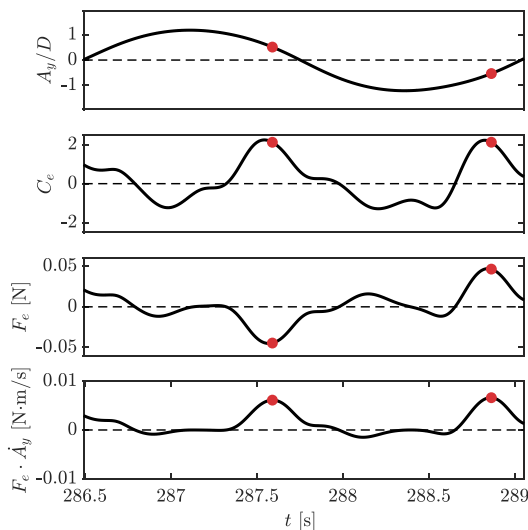


FIG. 30. Energy transfer due to vorticity dynamics for the 2T mode at $Vr = 7.00$. The parameters are the same as those in Ref. 1. Left: VIV response amplitude A_y/D , excitation C_e , excitation force F_e , and rate of energy transfer $F_e \cdot \dot{A}_y$ (from top to bottom). Right: instantaneous vorticity contours correspond to the red symbols in the time profiles on the left. Vortex images with the yellow background are the results in Ref. 1.

The result in the present study contains a higher harmonic component compared with the reference. Figure 29 shows the FFT results of the response amplitude, velocity, and amplitude. The response amplitude contains a slightly higher harmonic component, but the response acceleration contains a much higher harmonic component. Assuming that the CF response is a harmonic motion with a fundamental frequency and third harmonic component $y = A_1 \sin(2\pi ft) + A_2 \sin(6\pi ft)$, the acceleration can be expressed as $\ddot{y} = 4A_1(\pi f)^2 \sin(2\pi ft) + 36A_2(\pi f)^2 \sin(6\pi ft)$, which means that the acceleration will contain eight times the amplitude of the third harmonic component relative to the fundamental component. In Ref. 1, the authors separate the added mass force (called the potential added mass force in the reference) by assuming $F_m \sim y(t)$, which ignores the higher harmonic component. In the present study, the FFLS method is applied for a more accurate result.

The dominant frequency of the excitation coefficient is twice the displacement. Based on the proportionality related to trigonometric functions, the $2f$ excitation coefficient and f response velocity will induce a total force containing the $(2 + 1)f$ and $(2 - 1)f$ components. The second contour figure matches well with the experimental result: a peak energy income occurs when a clockwise vorticity moves downstream to the right, as the body moves downward. In addition, the first contour figure shows that peak energy dissipation occurs when an anticlockwise vorticity moves downstream to the right as the body moves downward.

The energy transfer in $Vr = 7.00$ is shown in Fig. 30. The contour plot matches well with the experiment. The result shows that there exist two peaks in one period, and the 2T mode occurs at the peak time, which agrees well with the analysis from a previous study.¹

In summary, we apply the FFLS algorithm to analyze the mechanism of VIV of an isolated bluff cylinder. Compared with the theoretical result, the energy peak obtained by the FFLS algorithm matches well and can reflect the multi-frequency characteristic.

REFERENCES

- ¹N. Jauvtis and C. Williamson, "The effect of two degrees of freedom on vortex-induced vibration at low mass and damping," *J. Fluid Mech.* **509**, 23–62 (2004).
- ²C. H. Williamson and A. Roshko, "Vortex formation in the wake of an oscillating cylinder," *J. Fluids Struct.* **2**, 355–381 (1988).
- ³R. Govardhan and C. Williamson, "Modes of vortex formation and frequency response of a freely vibrating cylinder," *J. Fluid Mech.* **420**, 85–130 (2000).
- ⁴J. Vandiver, L. Lee, S. Leverette, and H. Marcollo, *Shear7 User Guide* (Department of Ocean Engineering, Massachusetts Institute of Technology, Cambridge, MA, 2003).
- ⁵C. M. Larsen, K. Vikestad, R. Yttervik, E. Passano, and G. Baarholm, *VIVANA Theory Manual* (MARINTEK, Trondheim, Norway, 2001).
- ⁶J. K. Vandiver, "Dimensionless parameters important to the prediction of vortex-induced vibration of long, flexible cylinders in ocean currents," *J. Fluids Struct.* **7**, 423–455 (1993).
- ⁷A. Trim, H. Braaten, H. Lie, and M. Tognarelli, "Experimental investigation of vortex-induced vibration of long marine risers," *J. Fluids Struct.* **21**, 335–361 (2005).
- ⁸J. Chaplin, P. Bearman, Y. Cheng, E. Fontaine, J. Graham, K. Herfjord, F. H. Huarte, M. Isherwood, K. Lambrakos, C. Larsen *et al.*, "Blind predictions of laboratory measurements of vortex-induced vibrations of a tension riser," *J. Fluids Struct.* **21**, 25–40 (2005).
- ⁹R. Willden and J. Graham, "Numerical prediction of VIV on long flexible circular cylinders," *J. Fluids Struct.* **15**, 659–669 (2001).
- ¹⁰M. Tognarelli, S. Slocum, W. Frank, and R. Campbell, "VIV response of a long flexible cylinder in uniform and linearly sheared currents," in *Offshore Technology Conference* (OnePetro, 2004).
- ¹¹C. H. Williamson and R. Govardhan, "Vortex-induced vibrations," *Annu. Rev. Fluid Mech.* **36**, 413–455 (2004).
- ¹²T. Sarpkaya, "A critical review of the intrinsic nature of vortex-induced vibrations," *J. Fluids Struct.* **19**, 389–447 (2004).
- ¹³C. Williamson and R. Govardhan, "A brief review of recent results in vortex-induced vibrations," *J. Wind Eng. Ind. Aerodyn.* **96**, 713–735 (2008).
- ¹⁴X. Wu, F. Ge, and Y. Hong, "A review of recent studies on vortex-induced vibrations of long slender cylinders," *J. Fluids Struct.* **28**, 292–308 (2012).
- ¹⁵Z. Wang, D. Fan, and M. S. Triantafyllou, "Illuminating the complex role of the added mass during vortex induced vibration," *Phys. Fluids* **33**, 085120 (2021).
- ¹⁶L. Ma, K. Lin, D. Fan, J. Wang, and M. S. Triantafyllou, "Flexible cylinder flow-induced vibration," *Phys. Fluids* **34**, 011302 (2022).
- ¹⁷D. Sumner, "Two circular cylinders in cross-flow: A review," *J. Fluids Struct.* **26**, 849–899 (2010).
- ¹⁸M. Rastan and M. M. Alam, "Transition of wake flows past two circular or square cylinders in tandem," *Phys. Fluids* **33**, 081705 (2021).
- ¹⁹G. R. Assi, P. Bearman, and J. Meneghini, "On the wake-induced vibration of tandem circular cylinders: The vortex interaction excitation mechanism," *J. Fluid Mech.* **661**, 365–401 (2010).
- ²⁰G. R. Assi, "Wake-induced vibration of tandem and staggered cylinders with two degrees of freedom," *J. Fluids Struct.* **50**, 340–357 (2014).
- ²¹X. Shan, "Effect of an upstream cylinder on the wake dynamics of two tandem cylinders with different diameters at low Reynolds numbers," *Phys. Fluids* **33**, 083605 (2021).
- ²²S. Kim, M. M. Alam, H. Sakamoto, and Y. Zhou, "Flow-induced vibrations of two circular cylinders in tandem arrangement. Part I. Characteristics of vibration," *J. Wind Eng. Ind. Aerodyn.* **97**, 304–311 (2009).
- ²³L. Ding, M. M. Bernitsas, and E. S. Kim, "2D URANS vs. experiments of flow induced motions of two circular cylinders in tandem with passive turbulence control for $30\,000 < Re < 105\,000$," *Ocean Eng.* **72**, 429–440 (2013).
- ²⁴F. Huera-Huarte and P. Bearman, "Vortex and wake-induced vibrations of a tandem arrangement of two flexible circular cylinders with near wake interference," *J. Fluids Struct.* **27**, 193–211 (2011).
- ²⁵W. Wu, J. Wang, and Z. Hu, "Study on the flow-induced vibration of a two-tandem cylinder system in rigid body motion," *Phys. Fluids* **34**, 013302 (2022).
- ²⁶S. Huang and A. Sworn, "Interference between two stationary or elastically supported rigid circular cylinders of unequal diameters in tandem and staggered arrangements," *J. Offshore Mech. Arct. Eng.* **135**, 021803 (2013).
- ²⁷W. Xu, Q. Zhang, Y. Yu, J. Lai, and Y. Chang, "Fluid-structure interactions (FSI) behaviour of two unequal-diameter flexible cylinders in tandem configuration," *Ocean Eng.* **218**, 108148 (2020).
- ²⁸M. J. Janocha, M. C. Ong, P. R. Nyström, Z. Tu, G. Endal, and H. Stokholm, "Flow around two elastically-mounted cylinders with different diameters in tandem and staggered configurations in the subcritical Reynolds number regime," *Mar. Struct.* **76**, 102893 (2021).
- ²⁹M. Zhang, S. Fu, Z. Zhang, H. Ren, and Y. Xu, "Experimental investigation on vortex-induced vibration of dual pipes with unequal diameters in tandem," in *International Conference on Offshore Mechanics and Arctic Engineering* (American Society of Mechanical Engineers, 2020), Vol. 84409, p. V008T08A027.
- ³⁰X. Fu, Y. Xu, M. Zhang, H. Ren, B. Zhao, and S. Fu, "Numerical simulation of vortex-induced vibration of two tandem cylinders with different diameters under uniform flow," in *International Conference on Offshore Mechanics and Arctic Engineering* (American Society of Mechanical Engineers, 2020), Vol. 84409, p. V008T08A034a.
- ³¹F. R. Menter, M. Kuntz, and R. Langtry, "Ten years of industrial experience with the SST turbulence model," *Turbul. Heat Mass Transfer* **4**, 625–632 (2003).
- ³²C. J. Greenshields *et al.*, *OpenFOAM User Guide, Version 3* (OpenFOAM Foundation Ltd., 2015), p. 47.
- ³³N. T. Basse, "Scaling of global properties of fluctuating streamwise velocities in pipe flow: Impact of the viscous term," *Phys. Fluids* **33**, 125109 (2021).
- ³⁴F. R. Menter, "Two-equation eddy-viscosity turbulence models for engineering applications," *AIAA J.* **32**, 1598–1605 (1994).
- ³⁵M. Zhao and L. Cheng, "Numerical simulation of two-degree-of-freedom vortex-induced vibration of a circular cylinder close to a plane boundary," *J. Fluids Struct.* **27**, 1097–1110 (2011).
- ³⁶A. Khalak and C. Williamson, "Dynamics of a hydroelastic cylinder with very low mass and damping," *J. Fluids Struct.* **10**, 455–472 (1996).
- ³⁷F. Ding and T. Chen, "Performance bounds of forgetting factor least-squares algorithms for time-varying systems with finite measurement data," *IEEE Trans. Circuits Syst. I* **52**, 555–566 (2005).
- ³⁸T. Sarpkaya, "Transverse oscillations of a circular cylinder in uniform flow, Part 1. Revised," Technical Report No. ADA 273095, Naval Postgraduate School, Monterey, 1977.
- ³⁹Y. Bao, C. Huang, D. Zhou, J. Tu, and Z. Han, "Two-degree-of-freedom flow-induced vibrations on isolated and tandem cylinders with varying natural frequency ratios," *J. Fluids Struct.* **35**, 50–75 (2012).
- ⁴⁰M. Zhang, S. Fu, L. Song, X. Tang, and Y. He, "A time domain prediction method for the vortex-induced vibrations of a flexible riser," *Mar. Struct.* **59**, 458–481 (2018).
- ⁴¹J. Dahl, F. Hover, M. Triantafyllou, S. Dong, and G. E. Karniadakis, "Resonant vibrations of bluff bodies cause multivortex shedding and high frequency forces," *Phys. Rev. Lett.* **99**, 144503 (2007).